Applied Materials Today 52 (2026) 103394

Contents lists available at ScienceDirect

Applied Materials Today

journal homepage: www.elsevier.com/locate/apmt

Data-driven volumetric printing of biomimetic hydrogels enables control of interstitial flow and shear stress

Linda Maggi [a,b], Lena Stoecker [c,d], Laura Maria Vergani [e,f,*], Miguel Castilho [c,d,1], Federica Buccino [e,f,1]

[a] Department of Mechanical, Manufacturing, and Biomedical Engineering, School of Engineering, Trinity College, Dublin 2, Ireland
[b] Trinity Centre for Biomedical Engineering, Trinity Biomedical Sciences Institute, Trinity College, Dublin 2, Ireland
[c] Biomaterial Engineering & Biofabrication, Department of Biomedical Engineering, Eindhoven University of Technology, the Netherlands
[d] Institute for Complex Molecular Systems, Eindhoven University of Technology, the Netherlands
[e] Department of Mechanical Engineering (DMEC), Politecnico di Milano, Via La Masa 1, 20156 Milan, Italy
[f] IRCCS Galeazzi-Sant'Ambrogio, Via Cristina Belgioioso 173, 20157 Milan, Italy

ARTICLE INFO

Keywords:
Bone scaffolds
Generative design
Synchrotron micro-CT
Xolography
Computational Fluid Dynamics

ABSTRACT

Bone mesoscale architecture governs interstitial fluid dynamics, which regulate cell mechanotransduction and subsequent bone remodelling. However, how trabecular mesoscale features influence fluid flow and wall shear stress (WSS) conducive to osteogenesis remains poorly understood, particularly in osteoporotic bone. This study aims to clarify how osteoporosis-driven architectural deterioration alters fluid-induced mechanical cues and how these cues can be transferred into biomimetic models that enable in vitro investigation of cellular mechano-biological responses. Synchrotron radiation micro-computed tomography (SRμCT) datasets of human trabecular bone were used to extract key morphometric descriptors. Osteoporosis led to reduced bone volume fraction, increased trabecular spacing and higher anisotropy. These parameters informed a Voronoi-based design strategy to generate porous architectures with controlled mesoscale features. Scaffolds were fabricated via Xolography: a dual-colour volumetric printing process. Among four hydrogel formulations varying in ratios of polytheylene glycol diacrylate (PEGDA) and polyethylene glycol dimethacrylate (PEGDMA) which were functionalised with arginine-glycine-aspartic acid (RGD) peptides post-printing, the 30% w/w PEGDA and 10% w/w PEGDMA blend provided the best balance between processability and biological performance measured by metabolic activity. Computational fluid dynamics simulations under perfusion conditions demonstrated that architectural parameters directly govern permeability WSS, enabling access to osteogenic-relevant regimes at inlet velocities of 0.15–0.25 mm/s. The resulting scaffolds exhibited permeability values (3.54×10^{-8}–19.0×10^{-8} m^2) comparable to native bone, while distinct architectural configurations produced systematic variations in surface WSS. In particular, structures derived from osteoporotic morphologies displayed higher permeability but reduced WSS, highlighting the strong coupling between geometry and flow-mediated mechanical stimuli. These trends were consistent with simulations performed on native bone volumes, confirming the ability of the approach to preserve condition-specific flow signatures. Herein, this research establishes a data-driven design-to-fabrication strategy for volumetrically printed hydrogels, enabling programmable control of transport properties and shear stress.

1. Introduction

Bone tissue exhibits a remarkable regenerative capacity in case of damage, but this ability is compromised in cases of critical-sized defects and in individuals affected by osteoporosis [1,2]. Osteoporosis is a systemic skeletal disorder characterised by reduced bone mass and microarchitectural deterioration [3,4]. It is the most prevalent bone disease globally: it affects approximately one in three women and one in five men over the age of 50 worldwide [5]. Given the global demographic shift toward an aging population, the incidence of bone

* Corresponding author at: Department of Mechanical Engineering (DMEC), Politecnico di Milano, Via La Masa 1, 20156 Milan, Italy.
E-mail address: laura.vergani@polimi.it (L.M. Vergani).
[1] Co-last authors

https://doi.org/10.1016/j.apmt.2026.103394
Received 18 March 2026; Received in revised form 16 June 2026; Accepted 14 August 2026
Available online 22 August 2026

fractures constitutes a growing clinical and socioeconomic concern [4–8]. These challenges and the limits of current solutions have catalysed intensive research in bone tissue engineering (BTE), where scaffolds are developed both as implants and as in vitro models to investigate disease progression and treatment strategies.

Native cancellous bone exhibits a hierarchical architecture, with a lacuna-canalicular network at the microscale and trabecular architecture at the mesoscale. Morphological features (Fig. 1) of this mesoscale architecture can be evaluated by imaging methods such as computed tomography (CT) and magnetic resonance imaging (MRI) [9–12]. It is known that illnesses and extreme circumstances, like microgravity [11], impact bone morphology. The effect of osteoporosis on morphometric features at the mesoscale was examined in a few studies but shows contradictory results [9–13].

The trabecular architecture plays a crucial role in directing interstitial fluid flow (Fig. 1), which in turn regulates the mechanical environment experienced by resident cells. The geometry of trabeculae determines local flow patterns, influencing fluid velocity and the resulting wall shear stress (WSS) on bone surfaces. Most studies to date have focused on the lacuna-canalicular network, characterizing fluid flow sensed by osteocytes [14–16], while only a limited number of investigations have examined flow at the trabecular surfaces, where osteoblasts, osteoclasts, and mesenchymal stem cells (MSCs) reside [17–19]. In particular, fluid shear at these surfaces is mechanotransduced by MSCs, promoting osteogenic differentiation and extracellular matrix mineralization [20,21]. Although the mechanosensitivity of MSCs to WSS has been demonstrated in vitro [22,23], it remains largely unclear how alterations in trabecular architecture, particularly those associated with osteoporosis, modify interstitial fluid dynamics and consequently cellular behavior. Evidence is scarce: for example, Zhao et al. [24] reported reduced WSS in osteoporotic rat femurs compared to healthy controls. A decrease in WSS at the trabecular surface could compromise bone cell responses, potentially initiating a vicious cycle that accelerates bone loss in osteoporosis. This gap highlights the need for studies that directly link changes in human trabecular architecture to alterations in fluid flow and mechanotransduction.

Bone scaffolds could replicate or take inspiration from the trabecular structure to recreate the fluid dynamics present in natural bone, thereby serving as in vitro models for studying fluid dynamics. In order to do so, the choice of fabrication technique is pivotal for precise control over scaffold architecture. Among additive manufacturing modalities, photopolymerization methods represent state-of-the-art approaches for microscale scaffold fabrication. Two-photon polymerization (2PP) is notable for its ultra-high resolution, however its application is limited by inherently slow volumetric build rates [25]. In contrast, Computed Axial Lithography (CAL), as a volumetric printing process, enables accelerated printing of macroscopic structures but offers comparatively lower resolution [26]. Xolography, an emerging dual-color photopolymerization technique, addresses the speed-resolution trade-off by leveraging dual-color photoinitiators (DCPIs) activated through orthogonally intersecting light beams [26]. Xolography exhibits exceptional potential, offering rapid print times ranging from seconds to minutes (volume generation rates reach 55 mm^3/s), with spatial resolution on the order of 10 μm for acrylate-based resins [27]. This technology provides geometric freedom, potentially enabling replication of the bone's mesoscale architecture.

The choice of scaffold material is equally important. Hydrogels are widely favoured in tissue engineering for their biocompatibility, high water content and ability to mimic the extracellular matrix, promoting cell proliferation and differentiation [28,29]. Recent advances yield functional hydrogels [30] with stimuli-responsive properties [31,32], controlled drug release, cell recruitment, cell modulation [33,34] and immunomodulation [29] properties, alongside bioprinting strategies for precise cell-laden constructs [35–37]. Here, we employ Xolography-compatible hydrogels to fabricate scaffolds as an initial platform for in vitro fluid flow studies, providing foundational data to guide future enhancements toward implantability. Xolography's application with biocompatible hydrogels, while demonstrating promising

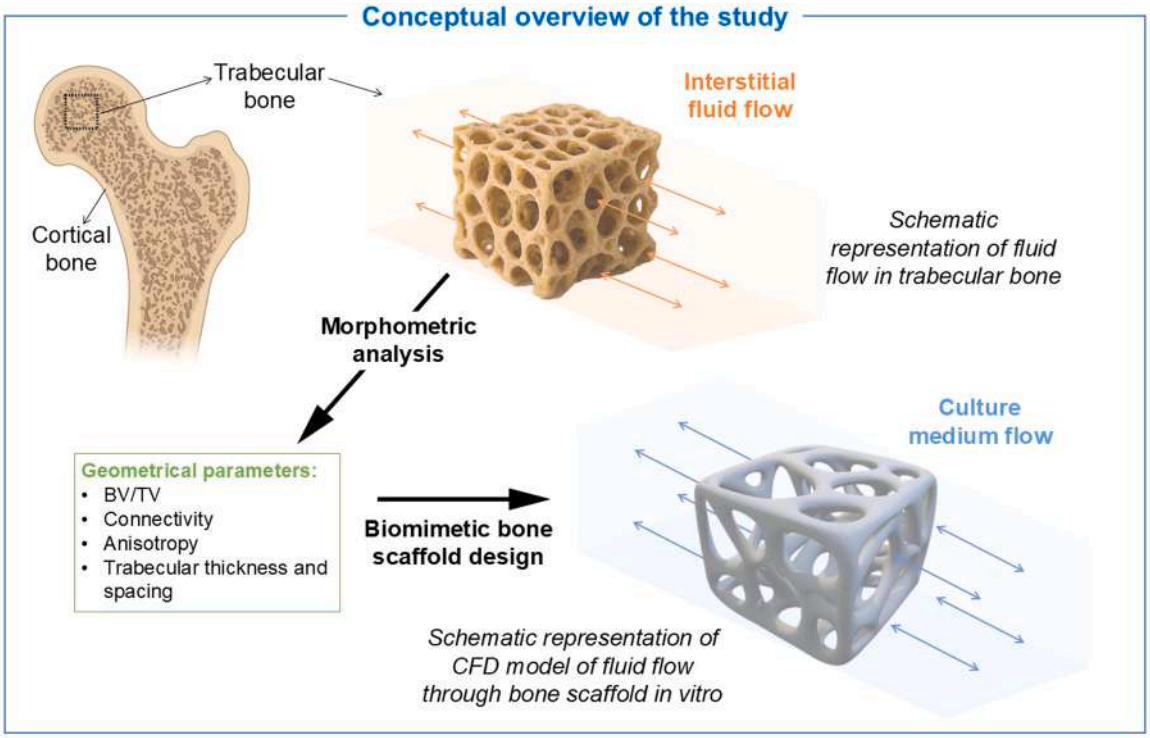

Fig. 1. Conceptual overview of the study. The aim of this work was to reproduce the interstitial fluid flow observed in native human bone in simplified in vitro models. Geometrical parameters were extracted from trabecular bone samples obtained from human femoral heads and subsequently translated into printable scaffold designs. The performance of the scaffolds in replicating the fluid flow was then evaluated with computational fluid dynamics (CFD) simulations.

results [28,38,39], remains nascent, with most reported examples based on GelMA or GelMA/PEGDA formulations, which present trade-offs between bioactivity and printability.

This study addresses the lack of consensus on how osteoporosis alters bone mesoscale architecture and interstitial fluid flow by providing synthetic bone scaffolds that reproduce the trabecular network of healthy and osteoporotic bone. These simplified models can eventually serve as a template for systematic investigation of fluid dynamics and mechanotransduction in vitro (Fig. 1). We hypothesise that replicating key geometrical features of trabeculae will generate WSS patterns that

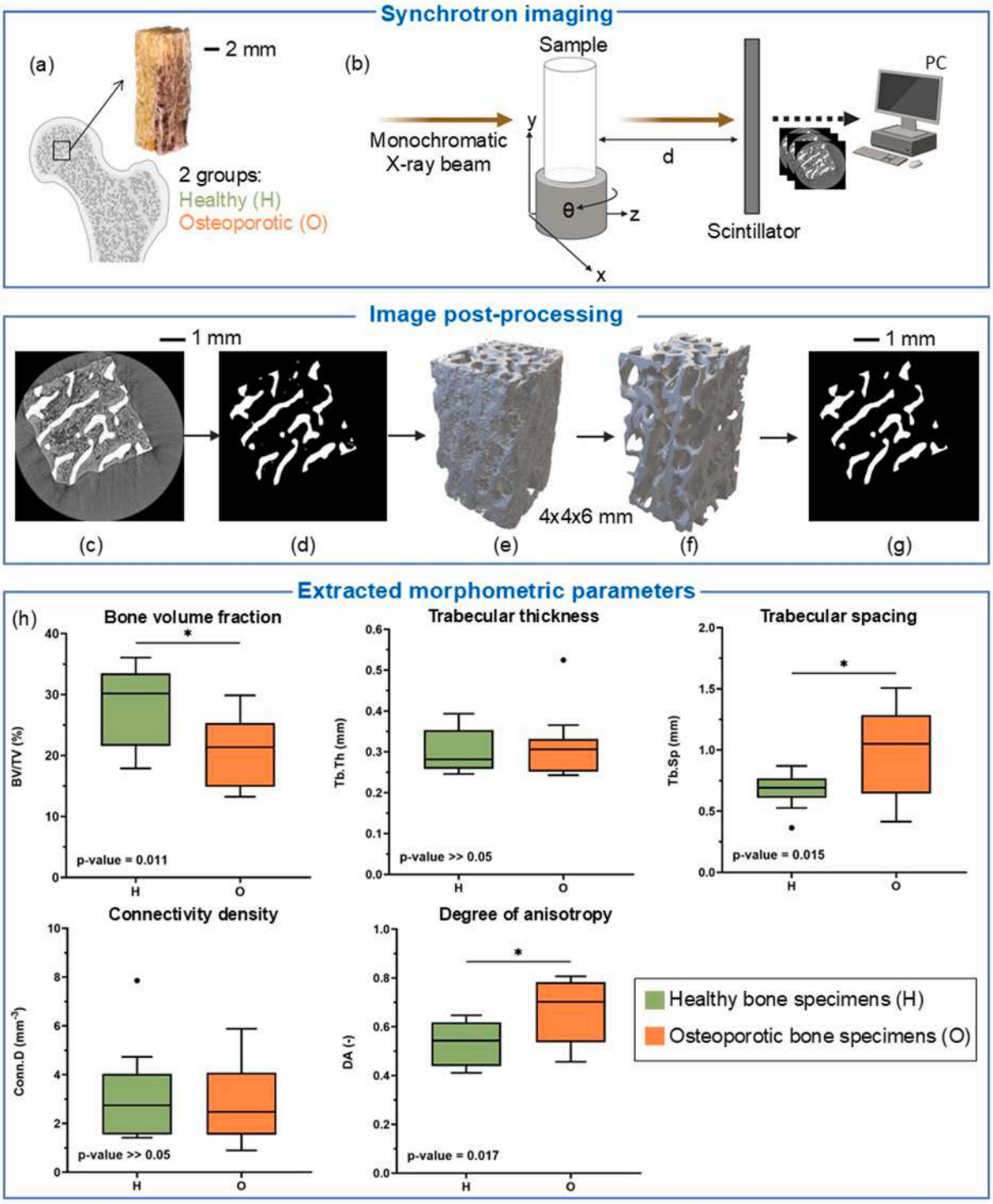

Fig. 2. Morphometric analysis of bone samples: from imaging to parameters extraction. (a) Twenty trabecular bone samples (4 × 4 × 6 mm) were harvested from femoral heads of healthy and osteoporotic patients undergoing hip arthroplasty. **(b)** SRμCT imaging setup, with projections acquired during 360° rotation of the sample. **(c)** Raw synchrotron image, **(d)** binarised image, **(e)** 3D reconstruction, **(f)** cleaned 3D model, **(g)** representative slice after filtering. **(h)** Extracted morphometric parameters: bone volume fraction (BV/TV), trabecular thickness (Tb.Th), trabecular spacing (Tb.Sp), connectivity density (Conn.D), and degree of anisotropy (DA). Comparisons between healthy (H) and osteoporotic (O) samples were performed using Welch's *t*-test or Mann–Whitney *U* test, depending on data normality. Statistical significance was defined as $p < 0.05$ (*).

differ between healthy and osteoporotic conditions and that these features and effects can be maintained in simplified and manufacturable scaffold designs. To test this, human bone morphometry was quantified from images obtained with Synchrotron Radiation Micro-Computed Tomography (SRμCT) and used to inform a generative scaffold design approach that preserved essential trabecular features. Xolography, as a state-of-the-art, high-resolution manufacturing method was employed to test and improve the printability of scaffold designs. To ensure durability under in vitro conditions, scaffold designs were printed from newly formulated synthetic hydrogels and mechanically tested for structural robustness and resistance to deformation or swelling. Taking advantage of computational fluid dynamics (CFD) simulations, the simplified scaffold designs were evaluated to determine whether they reproduce the interstitial fluid flow and WSS observed in native bone and to identify differences between healthy and osteoporotic conditions. These scaffolds provide a promising platform for in vitro investigation of MSC osteogenesis and for linking changes in trabecular architecture to alterations in fluid flow and mechanotransduction.

2. Materials and methods

2.1. Bone synchrotron scans analysis

2.1.1. Bone sample collection and imaging

Twenty trabecular bone samples, each measuring 4 × 4 × 6 mm, were obtained from the femoral heads of patients undergoing hip arthroplasty (Fig. 2a). Samples were sectioned along the principal tensile and compressive stress trajectories. The study was conducted with approval from the Ethics Committee of San Raffaele Hospital (Milan, Italy, approval date: 13/05/2020, ClinicalTrials.gov ID: NCT04787679), and all patients provided signed informed consent. Donors range in age from 58 to 88 years and include exclusively female patients. Ten samples were derived from osteoporotic patients, while ten were collected from patients without diagnosed osteoporosis (hereafter referred to as "healthy"). This classification followed bone mineral density measurements obtained via dual X-ray absorptiometry, according to the World Health Organization's 1994 criteria, where a T-score ≤ -2.5 defined osteoporosis [40]. Each bone specimen underwent imaging at the Elettra synchrotron facility (Trieste, Italy), specifically within the experimental hutch of the SYRMEP (SYnchrotron Radiation for MEdical Physics) beamline. SRμCT experiments (Fig. 2b) were conducted using a white-beam setup in propagation-based phase-contrast mode. Imaging was performed with a specimen-to-detector distance of 150 mm and an average X-ray energy of 25.6 keV, achieved using a 1.5 mm thick silicon attenuator. Projections were acquired using a 16-bit, water-cooled Orca Flash 4.0 sCMOS camera (2048 × 2048 pixels), optically coupled to a 17 μm thick GGG scintillator screen. Scans were executed in half-acquisition mode, involving a full 360° rotation of the specimen. The system provided an effective pixel size of 1.6 μm × 1.6 μm, corresponding to a field of view of 3.28 mm × 3.28 mm. Image acquisition was performed in continuous (fly-scan) mode with an exposure time of 50 ms per projection, yielding a total of 3600 projections per sample. Calibration was achieved through the acquisition of flat-field and dark-field reference images [41,42]. Raw projections were processed using a single-distance phase-retrieval algorithm to enhance contrast and reduce phase artifacts [43]. Three-dimensional volume reconstruction was then carried out using the filtered back projection (FBP) algorithm implemented in the SYRMEP Tomo Project (STP) software package [44].

The output images (Fig. 2c) underwent post-processing with a custom Matlab script (v2023b, MathWorks) outlined in [45,46]. This processing included artifact removal, stitching of sequential image stacks from multiple acquisitions into a single cohesive volume, and masking of the sample to isolate the region of interest. Given the study's focus on trabecular mesoscale architecture, only binarised images (Fig. 2d) were retained, and the number of slices per sample was downsampled to 974 to optimize computational efficiency. Subsequent 3D reconstructions using ImageJ (v 1.54 f, NIH) revealed the presence of debris and isolated fragments (Fig. 2e), which were removed using MeshLab (v2022.02, Visual Computing Lab of ISTI-CNR [47]). To further eliminate non-isolated debris, especially on the sample's outer shell, thin layers were trimmed from the four lateral faces employing Fusion 360 (v2.0.19994, Autodesk). The cleaning process with MeshLab was repeated as necessary (Fig. 2f). The final binarised image stacks (Fig. 2g) achieved a voxel resolution of 6.78 μm/pixel in the planar directions and 5.95 μm/pixel along the vertical axis.

2.1.2. Morphometric bone parameters

Five key morphometric parameters were extracted from the binarised two-dimensional slices of trabecular bone structures using BoneJ [48], an ImageJ plugin.

1. **Bone Volume Fraction (BV/TV):**
   This parameter quantified the proportion of mineralised bone volume (BV) relative to the total scanned volume (TV), expressed as a percentage (Eq.1):

$$Bone\ volume\ fraction\ (BV/TV) = \frac{Bone\ volume\ (BV)}{Total\ volume\ (TV)} \times 100 \quad [\%] \tag{1}$$

2. **Trabecular Thickness (Tb.Th):**
   Calculated using the local thickness algorithm developed by Hildebrand and Rüegsegger [49], this parameter defined the thickness at each point p within the bone structure as the diameter of the largest sphere that contains p and fits entirely within the trabecular region. This method provided a robust and geometry-independent measure of trabecular thickness, as described by Dougherty et al. [50].
3. **Trabecular Spacing (Tb.Sp):**
   Analogous to the Tb.Th computation, trabecular spacing measured the mean separation between trabeculae, corresponding to the dimensions of the marrow cavities. It was derived by applying the same local thickness model to the pore (non-bone) regions of the binarised structure.
4. **Connectivity Density (Conn.D):**

This metric quantified the number of interconnected trabecular elements per unit volume, reflecting the overall structural integrity of the network. Connectivity (Eq.2) was computed based on a modified Euler characteristic (χ), which is a topological invariant that described the number of connected components, loops, and cavities in a 3D structure:

$$Connectivity = 1 - (\chi + \Delta\chi) \tag{2}$$

where $\Delta\chi$ was a correction factor introduced to improve the accuracy of the connectivity estimation [51], [52]. The connectivity density is then defined as (Eq.3):

$$Connectivity\ density\ (Conn.D) = \frac{Connectivity}{Total\ volume\ \ (TV)} \quad [mm^{-3}] \tag{3}$$

i. **Degree of Anisotropy (DA):**

The DA described the orientation distribution of trabeculae, providing insight into the structural adaptation of bone to mechanical loading. It ranged from 0 (perfectly isotropic) to 1 (highly anisotropic with a dominant orientation). The DA was computed using the Mean Intercept Length (MIL) method, which statistically sampled line intercepts along multiple directions through the structure [53]. For this study, the following parameters were optimised for the MIL analysis: 2000 directions, 10,000 lines per direction, and a sampling increment of

$\sqrt{3}$.

The selected parameters were chosen to provide a complementary description of trabecular bone, as single parameters alone can be misleading [9]. BV/TV, Tb.Th and Tb.Sp are established descriptors of bone quality and structural changes in physio-pathological states [9,54,55], with BV/TV strongly correlated to bone macroscopic mechanical properties [56–58]. Conn.D and DA were included to capture architectural organization, which significantly influences mechanical behaviour [9,58,59]. This combined approach is widely supported for linking microstructure to bone quality [55,60].

2.2. Bone scaffold design

2.2.1. Voronoi tessellation and design workflow

The translation from natural bone hierarchical structure to engineered scaffold design relied on the Voronoi tessellation method, which consisted in the partition of a plane or space into regions based on a given set of points, referred to as "nucleating points" (n_s). This method generates regions, known as "Voronoi cells", which consist of all points closer to a specific seeding point than to any other [61]. Given a set of m points $P = \{P_1, p_2\ldots, p_m\}$ in a n-dimensional space, the Voronoi cell was mathematically defined as (Eq.4) [62,63]:

$$V_i = \left\{ x : \forall j \neq i, \quad d(x,p_i) \leq d\left(x,p_j\right) \right\}, i,j \in \{1,2,\ldots, \quad m\} \tag{4}$$

Where $d(x,y)$ represented the distance between two points, typically measured using the Euclidean distance. For points $x = (x_1, x_2\ldots, x_n)$ and $y = (y_1, y_2\ldots, y)$, the Euclidean distance was defined as (Eq.5):

$$d(x,y) = \quad \| x - y \|_2 = \sqrt{\sum_{k=1}^{n} (x_k - y_k)^2} \tag{5}$$

To generate biomimetic bone scaffolds with controllable geometric parameters, an interactive generative design workflow was implemented in Rhinoceros 8 (v8.10, Robert McNeel & Associates) using the Grasshopper plugin (v1.0.008). The inputs included a bounding box ($4 \times 4 \times 4$ mm) called region of interest (ROI), the number of nucleating points and a "generation" number to seed the points. The number of nucleating points was calculated to achieve a porosity compatible to that of native bone, using a simplified formula (Eq.6) adapted from Fantini et al. [64]:

$$n_s = \quad \frac{V_{void}}{\frac{4}{3}\pi\left(\frac{Tb.Sp}{2}\right)^3} \quad where\ V_{void} = V_{ROI} \times (1 - BV \Big/ TV) \tag{6}$$

Here, n_s is calculated by assuming all pores have a diameter equal to Tb.Sp, aiming for a geometry which has a porosity compatible with native bone (i.e., 1 – BV/TV). The values of Tb.Sp and BV/TV were derived from synchrotron-based microstructural analysis. V_{ROI} denotes the volume of the bounding box, while V_{void} is the volume of empty space within the box. The nucleating points were seeded within the bounding box, then the Voronoi tessellation was applied. To generate the final scaffold geometry, curved pipes were implemented around the tessellation edges and node radii and beam thicknesses were adjusted to match the BV/TV values extracted from healthy and osteoporotic bone scans. The final geometry was exported in STL format. To verify the morphological accuracy of the design, values of Tb.Th and Tb.Sp (that here referred to the struts of the scaffolds) were extracted from the STL files and compared with corresponding native bone values.

2.2.2. Geometry simplification

The scaffolds designed using nucleating point values derived from (Eq.6 required geometric simplification to align with the resolution limits of the herein used hydrogel material in combination with the Xolography process. High geometric complexity challenged both printability and structural integrity. To address this, the scaffold geometries were simplified by proportionally scaling the number of nucleating points (n_s). This was achieved by modifying the bounding box dimensions and decreasing the structural complexity. Two scaffold sizes along the order of magnitude of the scanned bone samples were selected: $7 \times 7 \times 3$ mm and $4 \times 4 \times 3$ mm. For each size, multiple values of n_s were tested using fixed scaling factors. The strut thickness was then carefully adjusted for each configuration to achieve a BV/TV consistent with that of native trabecular bone.

2.3. Xolography 3D printing

3D printing was carried out using a customised Xolography printer for research purposes, which operated on the same principles and included similar components as the commercially available Xube® (xolo GmbH, Berlin, Germany). It featured two light sources that projected a thin light sheet of 10–40 μm from 375 nm lasers, along with a visible light projector that produced a sequence of images of the sliced object into the light sheet.

Four distinct hydrogel formulations were prepared, each comprising two components in a 60:40 wt ratio (Component A: 60%; Component B: 40%). Component A consisted of a proprietary aqueous solution (xolo-PEGDA_Component-A, xolo GmbH), primarily composed of water, with triethanolamine (TEOA) and polyacrylic acid (PAA) as solutes. Component B was formulated by blending the DCPI JLe−145 (xolo GmbH) with the crosslinking agents PEGDA (Mw = 700 g/mol) and/or PEGDMA (Mw = 750 g/mol), both obtained from Sigma-Aldrich. The four hydrogel variants differed in the PEGDA:PEGDMA ratio and were prepared following protocols described in Stoecker et al. [28].

After printing, the samples were rinsed with phosphate-buffered saline (PBS) to remove unpolymerised material. The materials' refractive indices were measured using an Abbe refractometer (Optika Microscopes, Italy). For each formulation, the input parameters of light source intensity (I), printing speed (S) and energy (E) are interdependent according to the relationship provided by (Eq.7):

$$E = \quad \frac{3I}{S} \tag{7}$$

These parameters were optimised by systematically screening combinations of I and S to identify a feasible processing window that ensured adequate curing while maximizing resolution. This procedure was applied consistently across all four material combinations. To assess print fidelity and resolution, a benchmark test object was designed, incorporating features with pore diameters comparable to the native Tb.Sp and strut widths within the range of Tb.Th. The printed scaffolds were examined using a digital microscope (Keyence VHX-500F), and dimensional accuracy was evaluated by comparing printed geometries with the corresponding STL files using ImageJ. For each hydrogel formulation, 8 replicate samples were printed and analysed.

2.4. Mechanical characterization

2.4.1. Swelling test

Swelling behavior was assessed using 3D-printed cylindrical samples (5 mm diameter × 2.5 mm height), with five replicates (n = 5) per material formulation. Immediately after printing, each sample was positioned on a glass slide, and images were acquired using a digital microscope from the top and two opposing lateral views to establish baseline dimensions. The samples were then fully immersed in PBS and incubated in a light-protected environment at 37 °C to simulate physiological conditions.

Microscopic images were collected at predetermined time points (days 0, 1, 4, 7, 14, and 21). Dimensional measurements (diameter and height) were extracted using ImageJ software to calculate the sample volume at each time point (V_t). The volumetric swelling fraction (Eq.8) was then determined using the initial volume (V_0) as a reference:

$$\text{Volumetric swelling fraction} = SF_V = \frac{V_t}{V_0} \quad (8)$$

2.4.2. Compression test

Compression tests were conducted using the MicroTester G2 (CellScale) on cylindrical printed samples (5 mm diameter × 2.5 mm height) immersed in PBS (n = 4 for each material combination). The device applied a gradual displacement to the samples through a 6 mm^2 metallic plate glued to one end of a microbeam. The diameter of the microbeam was selected based on the specific sample stiffness to minimize deflection and ensure accurate force transmission. Each sample was compressed to 10% of its initial height over a 60-second ramp, corresponding to a displacement rate of approximately 0.25 mm/min. Although slower than typical compression rates used for hydrogels, this controlled speed mitigated lateral slipping, enhancing measurement reliability. The compression test provided an estimation of the material's stiffness, quantified by the Young's modulus E, derived as the slope of the linear region of the stress–strain curve. The quality of the linear fit was assessed using the coefficient of determination (R^2, considered acceptable if $R^2 \geq 0.98$) and the residual standard error (RSE), which must be < 5% of the stress values within the linear range to be deemed reliable.

2.4.3. Microindentation test

While compression was performed to assess the bulk mechanical properties of the samples, microindentation testing was employed to characterize local mechanical responses at discrete positions across the material and determine possible inhomogeneities. Cylindrical samples (5 mm diameter × 2.5 mm height) were used. Microindentation was carried out using the MicroTester G2 system, with samples submerged in PBS. A spherical indenter bead with a diameter of 1 mm applied a displacement equal to 10% of the initial sample height over a ramp duration of 60 s. For each material formulation, six samples were tested, and stress–strain data were collected at five distinct positions per sample, maintaining a minimum spacing of 15 μm between indentations, as recommended in [65].

Indentation data were analysed using the Hertz contact model (Eq.9), which describes the interaction between a spherical indenter and an elastic body under small deformation conditions:

$$F = \frac{4\sqrt{R}}{3} \frac{E}{1-\nu^2} d^{3/2} \quad (9)$$

where F is the indentation force, R is the indenter radius, E is the Young's modulus, ν is the Poisson's ratio and d is the indentation depth. A custom Matlab script, adapted from Huth et al. [65], was used to process the force–distance data and extract the local Young's modulus. To account for depth-dependent variations, the algorithm evaluated the modulus across the force–distance curve and plotted E as a function of indentation depth. The representative modulus was selected from the plateau region, corresponding to the best fit of the Hertzian model, thereby ensuring reliable and reproducible measurements of local stiffness.

2.5. Biological characterization

Human mesenchymal stem cells (hMSCs, obtained by human bone marrow of a healthy adult male donor, 1M0125, Lonza, USA; collected under their institutional guidelines and with informed consent; experiments were performed at Eindhoven University of Technology according to Dutch occupational health legislation) were used for the biological characterization of printed scaffolds. To ensure sufficient cell numbers, hMSCs were expanded in vitro in high-glucose Dulbecco's Modified Eagle Medium (DMEM; Gibco, Fisher Scientific) supplemented with pyruvate and L-glutamine, 10% fetal bovine serum (FBS; Serana Europe GmbH), 1% antibiotic-antimycotic (penicillin-streptomycin-amphotericin B; Gibco), non-essential amino acids (Gibco), and basic fibroblast growth factor (bFGF). Prior to scaffold testing, the optimal cell seeding density was calibrated to (i) avoid adverse effects associated with either under- or over-seeding and (ii) establish the linear range between seeding density and metabolic activity measured via the PrestoBlue assay (Invitrogen). A seeding density of 6000 cells/cm^2 was selected accordingly. For each material formulation, six samples were printed in a well-like geometry tailored to fit a standard 96-well plate. Each sample included a central circular cavity to ensure cell contact with the material and prevent lateral migration toward the well bottom. Sterilization was performed by ultraviolet (UV) irradiation for 15 min, followed by immersion in 70% ethanol for 30 min and triple rinsing with sterile PBS. Half of the scaffolds (n = 3 per material) underwent surface functionalization with RGD peptides (GRGDSPC, Mw = 690 g/mol; GenScript) at a concentration of 10 mM in PBS. The sterilization and functionalization protocols followed the methodology reported by Anindita et al. [66]. Samples were incubated overnight on an orbital shaker under light-protected conditions to ensure uniform peptide adsorption, followed by three PBS washes to remove unbound RGD. Cell metabolic activity was assessed using the PrestoBlue assay on day 6, with culture medium refreshed every two days.

2.6. CFD simulations

The STL files of the designed bone scaffolds were imported into COMSOL Multiphysics® software (v.6.2, COMSOL AB, Stockholm, Sweden) to perform CFD simulations. The analyses assumed a laminar and stationary Navier-Stokes model, as well as the incompressibility of the fluid. The governing equations (Eq.10) and (Eq.11) were:

$$\rho \frac{\partial u}{\partial t} + \rho(u \bullet \nabla)u = -\nabla p + \mu \nabla^2 u + f \quad (10)$$

$$\nabla \bullet u = 0 \quad (11)$$

where ρ is the fluid density, u is the fluid velocity, t is the time, p is the pressure, μ is the hydrodynamic viscosity and f is the force. (Eq.10) represents the conservation of momentum and (Eq.11) denotes the conservation of mass. DMEM was chosen as the fluid material to simulate the cell culture setting, with a hydrodynamic viscosity of 1.45 mPa·s and a density of 1 g/cm^3 [67]. The scaffold walls were considered hydrophilic and of no-slip nature, based on swelling tests which confirmed the materials' impermeability: this justifies neglecting internal permeation, consistent with prior CFD studies on dense hydrogels where flow is confined to scaffold pores [68,69]. As for boundary conditions, along the z-axis, the top face was considered as the fluid inlet with a velocity in the range commonly used by pumps in bioreactors while the bottom face is set as the fluid outlet with zero output pressure [62,67]. A mesh convergence analysis was performed using physics-controlled tetrahedral meshes by monitoring the mean and maximum WSS on the scaffold surface. Mesh convergence was considered achieved when the variation in both quantities between successive mesh refinements was below 1%. Depending on the scaffold geometry, convergence was reached using meshes containing between 439,748 and 1,998,432 elements.

To compare the mechanobiological behavior of the designed scaffolds with that of native trabecular bone, CFD simulations were also conducted on bone sub-volumes extracted from SRμCT datasets. Four representative samples were selected from each group (healthy and osteoporotic), based on BV/TV values close to the average of their respective populations. Each sub-volume was cropped to a size of $4 \times 4 \times 3$ mm^3, matching the dimensions of the designed bone scaffolds to enable direct comparison. Mesh generation and simulation conditions were aligned with those detailed for the scaffold geometries, reproducing perfusion-like flow environments representative of in vitro bioreactor settings.

2.7. Statistical analyses

The normality of the datasets (comprising geometrical parameters extracted from bone scans, results from compression and micro-indentation tests, and cell metabolic activity measurements from the PrestoBlue assay) was assessed using the Shapiro-Wilk test. For pairwise group comparisons, a Welch's *t*-test was applied when both groups exhibited normally distributed data; otherwise, a non-parametric Mann-Whitney *U* test was employed. Statistical significance was defined at two thresholds: $p < 0.05$ (*) and $p < 0.01$ (**). All statistical analyses were conducted using Matlab and GraphPad Prism (v.10.3.1, GraphPad Software, USA).

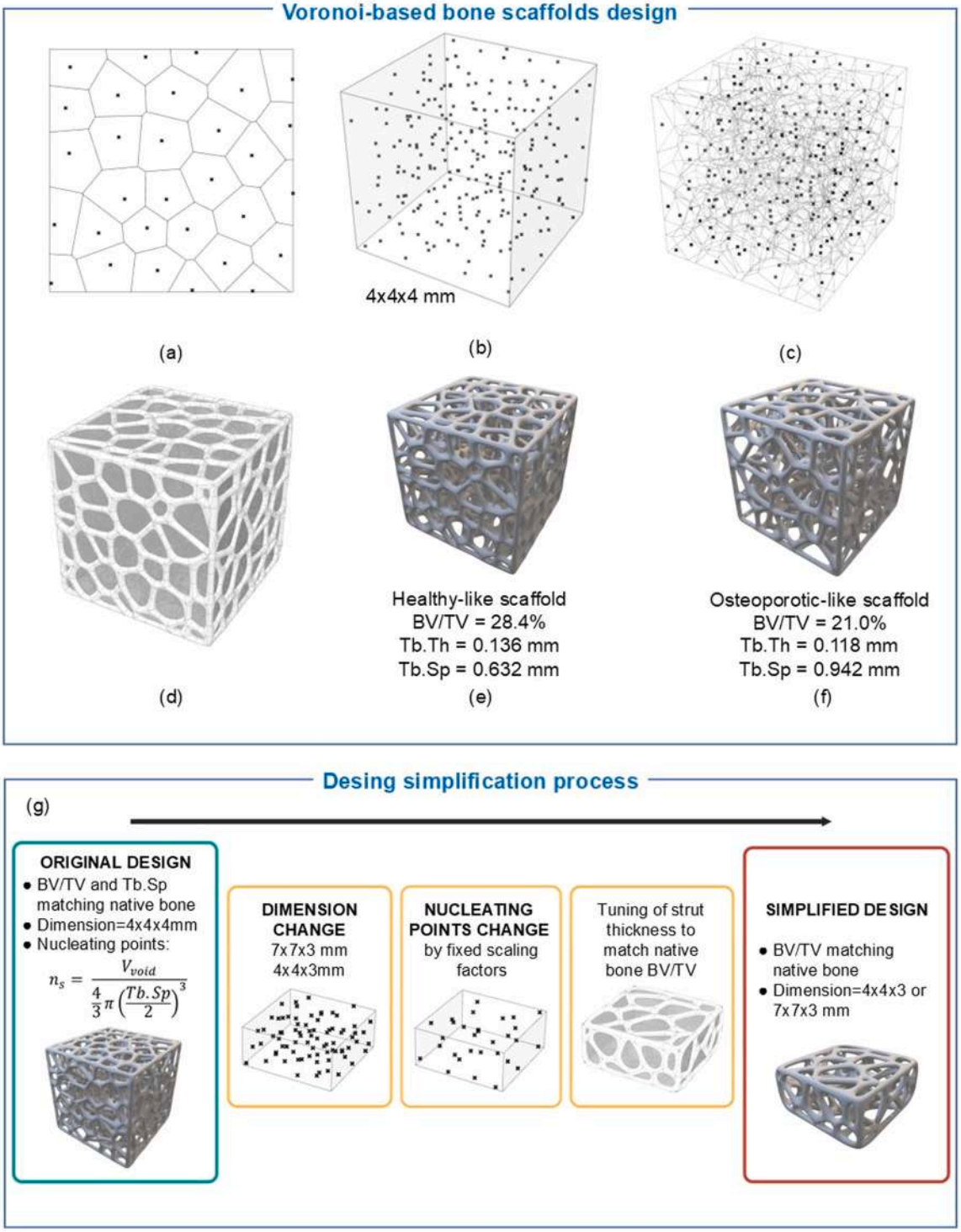

Fig. 3. Voronoi-based design for trabecular bone scaffolds. Voronoi tessellation can be applied to randomly distributed nucleating points (n_s), both in (a) 2D and (b–c) 3D domains. (d) Curved struts are generated along the tessellation edges, and both node radii and beam thicknesses are tuned to reproduce the bone volume fraction (BV/TV) and trabecular spacing (Tb.Sp) observed in synchrotron-derived structures from **(e)** healthy and **(f)** osteoporotic bone. **(g)** To ensure printability, a simplification process is applied: the scaffold volume is adjusted (e.g., from $4 \times 4 \times 4$ mm to $7 \times 7 \times 3$ mm or $4 \times 4 \times 3$ mm), and the number of nucleating points is reduced. The simplified designs retain BV/TV values consistent with those of the native healthy and osteoporotic bone.

3. Results

3.1. Computational generative design of bone-mimetic scaffolds

The study groups were well-matched for age, with no significant difference observed between the healthy (74.6 ± 5.6 years) and osteoporotic (75.8 ± 8.4 years) donors ($p = 0.74$). Furthermore, Pearson correlation analysis confirmed that donor age was not a significant confounding factor for any measured morphometric parameter (all $p > 0.11$, $r < 0.57$), indicating that observed differences are primarily attributable to the disease state.

The morphometric features are presented in Fig. 2h. BV/TV was significantly reduced in osteoporotic samples ($p = 0.011$), with the mean decreasing from 28.4% ± 6.2% in healthy (H) to 21.0% ± 5.5% in osteoporotic (O) specimens. Tb.Th showed no statistically significant difference between groups, with mean values of 0.301± 0.051 mm in healthy and 0.314 ± 0.084 mm in osteoporotic bone. However, notable intra- and inter-sample variability was observed, with some samples exhibiting abnormally large trabeculae that influenced the mean. Tb.Sp was significantly higher in osteoporotic bone (1.008 ± 0.344 mm) compared to healthy bone (0.673 ± 0.145 mm, $p = 0.015$), suggesting a more porous structure. The density of connected trabecular elements was marginally lower in osteoporotic samples (2.90 ± 1.74 structures/mm^3) than in healthy samples (3.15 ± 1.96 structures/mm^3), though not significantly. Finally, the DA was significantly elevated in osteoporotic bone (0.664 ± 0.127 vs. 0.534 ± 0.089, $p = 0.017$), with most values exceeding 0.45, indicating a pronounced preferential orientation of trabecular elements.

The translation of the structure of native bone into engineered scaffold geometries was achieved using Voronoi tessellation, an approach that can be applied to both 2D (Figs. 3a) and 3D (Fig. 3b-c) representations. Scaffold design was implemented through a generative workflow. The number of nucleating points was calculated to achieve porosity values compatible with those of native bone, as detailed in 2.2.1. These points were randomly seeded within the defined region of interest, a 4 × 4 × 4 mm bounding box (Fig. 3b), and Voronoi tessellation was then applied to generate a scaffold framework (Fig. 3c). Curved struts were formed along the tessellation edges (Fig. 3d), and both node radii and beam thicknesses were tuned to replicate the BV/TV observed in healthy (Fig. 3e) and osteoporotic (Fig. 3f) synchrotron trabecular structures.

Following the generative design process, the geometric properties were quantitatively extracted from the generated scaffolds and compared to the target native bone parameters (Table 1). The resulting scaffolds retained a trabecular-like topology characterised by interconnected, beam-like struts (Fig. 3d-e-f). Notably, both the healthy and osteoporotic scaffold variants exhibit similar Tb.Sp and smaller Tb.Th than their native counterparts.

The geometries were simplified to ensure successful printability, changing the overall size and the number of nucleating points (Fig. 3g). The resulting designs are shown in Fig. 4a. Reducing the number of nucleating points led to less intricate architectures, enabling more robust and reproducible fabrication.

Comparing the geometrical parameters of the bone scaffolds and the native bone specimens, in both healthy and osteoporotic cases, the simplified scaffold variants exhibited strut thicknesses from 24.2% to 212.0% greater compared to native bone (Fig. 4b), a necessary adjustment to meet manufacturing constraints. As expected, increasing the number of nucleating points resulted in thinner struts, since more complex geometries required reduced thickness to preserve the target BV/TV. This inverse relationship displayed a shallower slope in larger scaffolds (7 × 7 × 3 mm) compared to smaller ones (4 × 4 × 3 mm), meaning that for a given number of nucleating points, struts in larger scaffolds were generally thicker. Within each scaffold size, healthy bone-mimetic designs consistently presented higher strut thickness than osteoporotic counterparts, in accordance with their higher BV/TV. A similar trend was observed for pore spacing (Fig. 4c): increased geometric complexity, driven by a higher number of nucleating points, correlated with reduced spacing due to a denser network of struts. Larger scaffolds exhibited greater spacing. Healthy scaffolds showed lower spacing than osteoporotic ones, again reflecting the higher BV/TV of the healthy group.

3.2. Xolography-based 3D printing: photopolymer formulation

Scaffolds were fabricated using light-sheet xolography volumetric printing, whose working principle is shown in Fig. 5a: polymerization of photocrosslinkable polymers occurred inside a resin-filled cuvette at the intersection of a UV light sheet and visible light projections, enabled by the presence of a DCPI. Four PEG -based formulation were tested: 40%

Table 1
Geometrical comparison between Voronoi-based scaffold designs and native trabecular bone. Parameters include bone volume fraction (BV/TV), trabecular thickness (Tb.Th), and trabecular spacing (Tb.Sp). The number of nucleating points (n_s) in the designs is adjusted to replicate the BV/TV and approximate the Tb.Sp of healthy and osteoporotic bone specimens.

Healthy				Osteoporotic			
	BV/TV (%)	Tb.Th (mm)	Tb.Sp (mm)		BV/TV (%)	Tb.Th (mm)	Tb.Sp (mm)
Native bone	28.448	0.301	0.673	**Native bone**	21.044	0.314	1.008
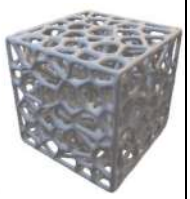 **n_s = 287**	28.472*	0.136°	0.632°	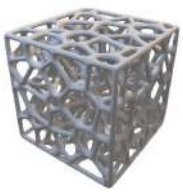 **n_s = 94**	20.946*	0.118°	0.942°

* values adjusted during the design process to match with native bone values
° values measured after the design process

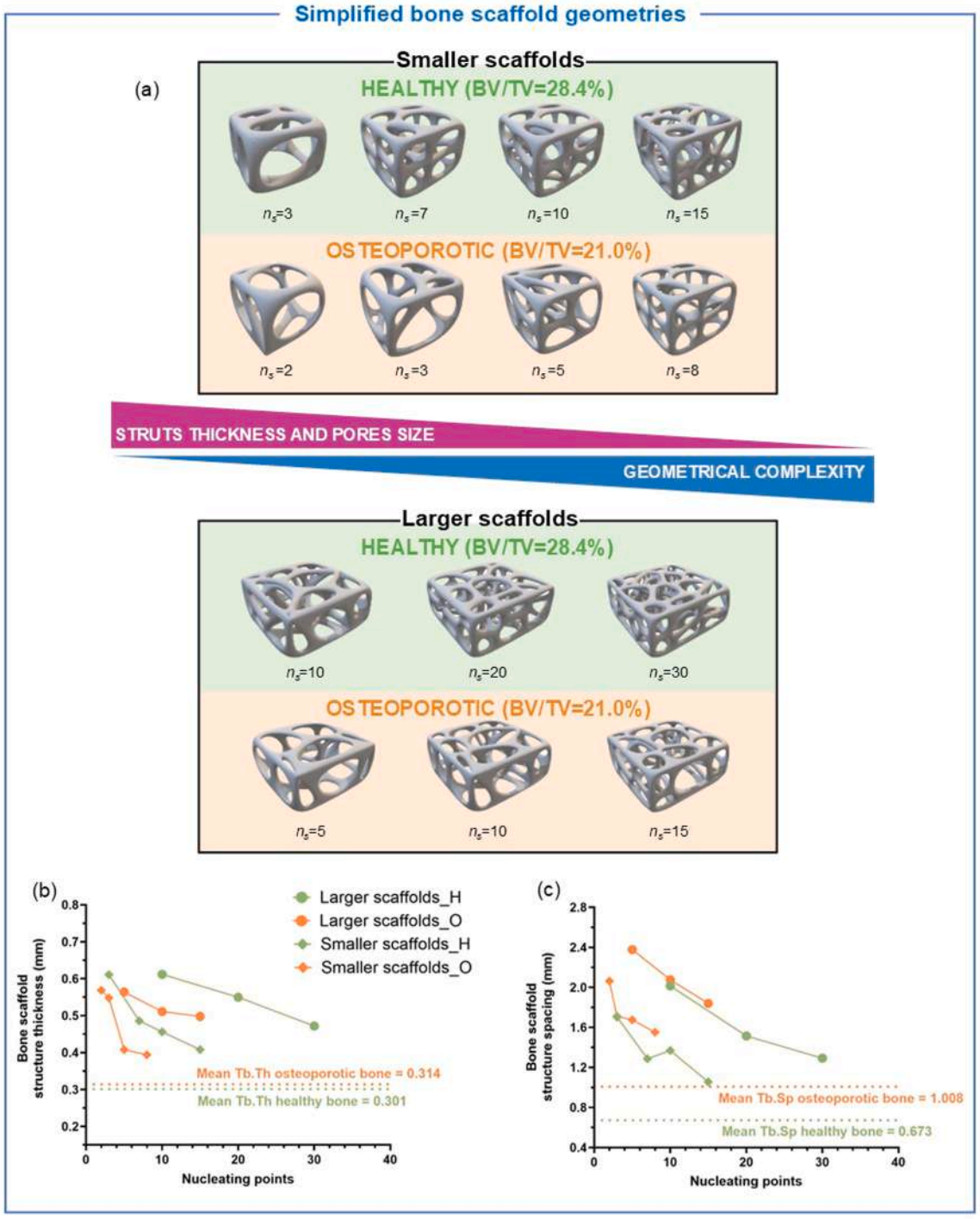

Fig. 4. Parametric simplification of scaffold architecture for enhanced manufacturability. (a) Scaffold geometries generated via Voronoi-based design for two characteristic sizes and two bone conditions (healthy and osteoporotic). For each condition, structural complexity was modulated by varying the number of nucleation points (n_s), enabling controlled simplification while maintaining the target bone volume fraction (BV/TV). **(b)** Quantitative analysis of average strut thickness as a function of nucleation points for healthy (H) and osteoporotic (O) groups, categorised by scaffold size. Increased geometric simplification (lower n_s) results in thicker struts, improving printability and mechanical robustness. **(c)** Average pore spacing as a function of nucleation points for each group and scaffold size. Larger pores are associated with lower n_s values, supporting enhanced mass transport while preserving morphometric fidelity to native bone.

PEGDA, 30% PEGDA–10% PEGDMA, 20% PEGDA–20% PEGDMA, and 40% PEGDMA (Fig. 5b). At high PEGDMA content, structures exhibited a visible loss of geometric fidelity; therefore 10% PEGDA–30% PEGDMA formulation was excluded. The formulation-specific printing parameters were optimised through iterative experimentation, serving as baseline conditions to be fine-tuned at each printing session to account for procedural variability and resin handling. The 40% PEGDA and 30% PEGDA–10% PEGDMA blends exhibited broad process windows and high reproducibility, while PEGDMA-rich formulations showed narrow windows and poor fidelity (Fig. 5c).

Resolution was assessed using a standardised test structure with beams (0.5–0.1 mm) and pores (1.0–0.6 mm) representative of the characteristic struts and voids of porous scaffolds (Fig. 5d). None of the formulations consistently printed beams < 0.3 mm, while beams

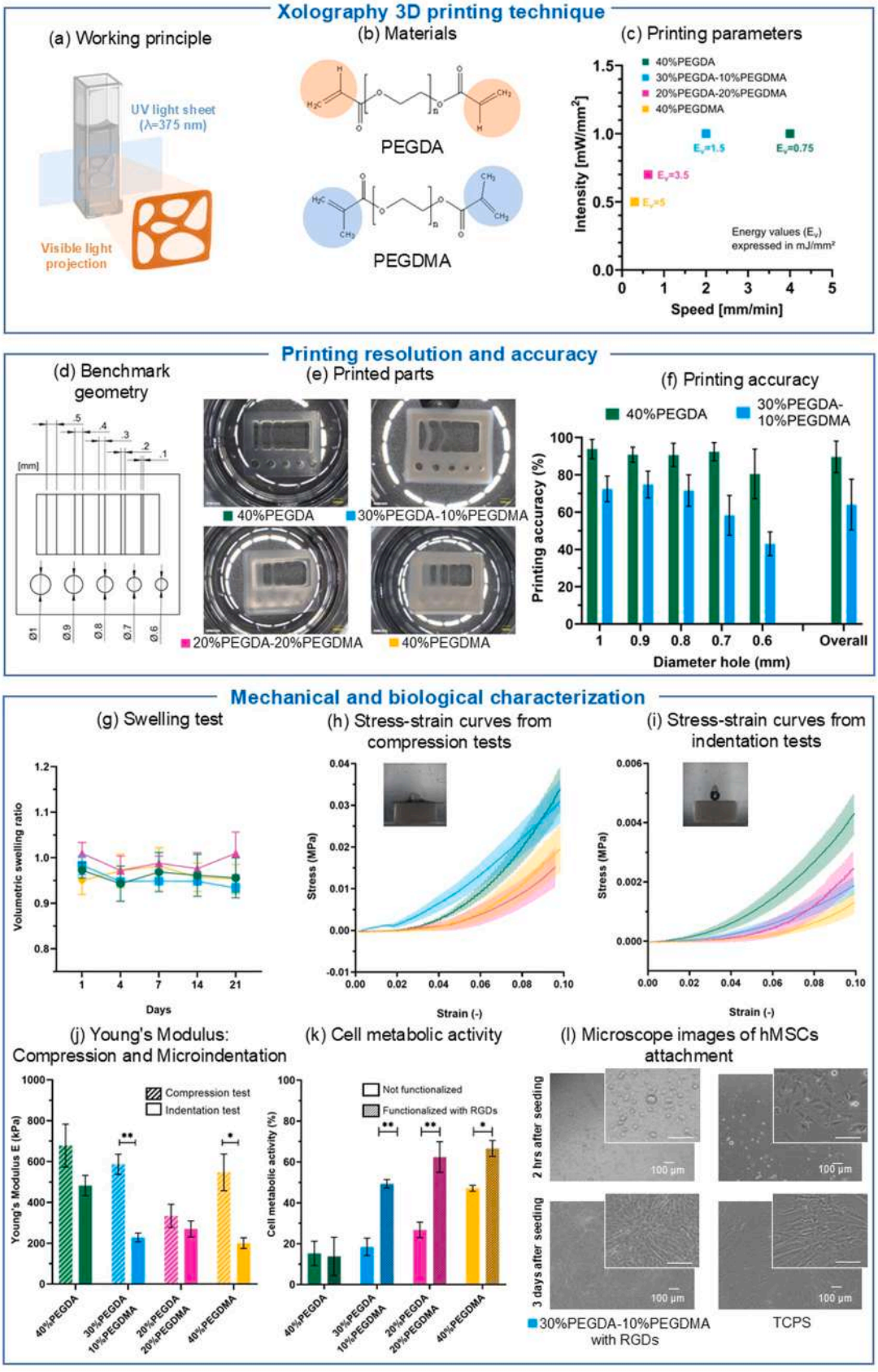

(caption on next page)

Fig. 5. Manufacturing method: Xolography working principle and characterization of PEGDA/PEGDMA-based printing formulations. (a) Schematic representation of the Xolography working principle within the resin-filled cuvette. (b) Chemical structures of the primary photocrosslinkable monomers: polyethylene glycol diacrylate (PEGDA) and polyethylene glycol dimethacrylate (PEGDMA), used in the development of hydrogel-based printing resins. **(c)** Four resin formulations with varying PEGDA/PEGDMA ratios are evaluated for printability and resolution. **(d)** CAD model of the resolution benchmark used to assess Xolography precision. **(e)** Representative printed resolution benchmarks for each tested formulation. **(f)** Quantitative evaluation of printing accuracy for two formulations: 40% PEGDA and 30% PEGDA–10% PEGDMA, based on dimensional fidelity of benchmark hole features. **(g)** Swelling behavior of the four hydrogel formulations over 21 days in PBS. **(h-i)** Stress–strain curves from uniaxial compression tests and from microindentation. **(j)** Quantitative comparison of Young's modulus values obtained from compression and indentation tests, reflecting material stiffness. **(k)** Cell metabolic activity of cells seeded on the resins with and without RGD functionalization. **(l)** Microscope images of human mesenchymal stem cells (hMSCs) attachment on 30% PEGDA – 10% PEGDMA functionalised with RGDs and on standard tissue culture polystyrene (TCPS). Significance thresholds are set at $p < 0.05$ (*) and $p < 0.01$ (**).

between 0.3–0.5 mm were unstable (Fig. 5e). Hole fidelity was therefore used as the primary metric (Fig. 5f). The 40% PEGDA and 30% PEGDA–10% PEGDMA formulations successfully printed the full range of feature sizes, whereas the 20% PEGDA–20% PEGDMA and 40% PEGDMA formulations failed to reproduce any of the designed pore dimensions. Across all samples, printed pores consistently deviated toward smaller-than-intended diameters, with accuracy inversely correlated to feature size. The 40% PEGDA formulation demonstrated the highest mean dimensional fidelity (89.7%), followed by 30% PEGDA–10% PEGDMA (64.0%). Overall, an increase in PEGDMA content was inversely correlated with printing resolution and dimensional accuracy.

3.3. Mechanical characterization

The mechanical characterization of the photopolymer formulations was considered to evaluate their suitability for future use in in vitro experiments by determining whether the materials can withstand sample handling and maintain geometrical stability without swelling.

Volumetric swelling ratios remained close to unity across all formulations over both short-term (1–7 days) and long-term (14–21 days) immersion periods (Fig. 5g). Minor shape deviations and slight measurement variability observed during sample handling and imaging occurred but did not indicate substantial swelling or degradation, confirming the materials' dimensional stability under aqueous conditions.

The Young's modulus E of the four photopolymer formulations was evaluated using complementary mechanical testing methods: compression testing and microindentation. Stress-strain curves from both modalities are presented in Fig. 5h-i, with the extracted moduli summarised in Fig. 5j. Notably, significant discrepancies between compression and microindentation results were observed for the 30%PEGDA–10% PEGDMA and 40%PEGDMA formulations, with microindentation consistently yielding lower moduli, likely reflecting local heterogeneities or surface effects. Generally, the stiffness measured by compression decreases as PEGDMA content increases, except for the 40%PEGDMA formulation, which exhibited anomalously higher stiffness. Across all formulations, average modulus values ranged from 201 to 678 kPa.

3.4. Biological characterization

Cell metabolic activity data assessed at day 6 post-seeding were normalised to a control consisting of cells cultured on standard tissue culture polystyrene (TCPS), representing an ideal substrate for cell growth under in vitro conditions (Fig. 5k).

Measured metabolic activity increased with increasing percentage of PEGDMA but remained far below the control group, which was potentially due to a lack of cell adhesion sites. Functionalization of the scaffolds with bioactive peptides therefore aimed to enhance cellular interactions by providing specific adhesion motifs. For the 40% PEGDA formulation, functionalization did not yield a statistically significant improvement in cell metabolic activity, suggesting limited peptide conjugation and thereby insufficient presence of bioactive sites. However, in formulations containing PEGDMA, which inherently offered a higher density of methacrylate groups available for covalent peptide attachment, functionalization led to a notable increase in cell metabolic activity. Overall, the highest relative cell metabolic activity observed was approximately 65% compared to TCPS. High cell viability for hMSCs seeded on a similar combination of PEGDMA and PEGDA has been previously reported by Anindita et al. [66].

To ensure sufficient presence of cells for the formulation containing low PEGDA ratios, microscope images of hMSCs seeded on 30% PEGDA–10% PEGDMA functionalised with RGDs (Fig. 5l) show that, compared to TCPS, cells still appear rounded 2 h after seeding and poorly spread. However, after 2 days, cells were elongated, indicating sufficient presence of available binding sites.

3.5. Xolography-based 3D printing of bone-mimetic scaffolds

The 30%PEGDA–10%PEGDMA formulation was selected for scaffold fabrication, as it provided a compromise between print resolution and adequate metabolic activity. Initial attempts to fabricate $4 \times 4 \times 4$ mm scaffolds without simplifications proved unsuccessful. These designs, while morphologically accurate, resulted in uncontrolled polymerization within the internal pore network during the volumetric exposure process, ultimately producing occluded and non-perfusable structures. To address this limitation, geometrical simplifications were introduced. With these adapted designs, scaffolds from the healthy bone group were successfully printed in both the smaller ($4 \times 4 \times 3$ mm) and larger ($7 \times 7 \times 3$ mm) formats (Fig. 6a–b). Fig. 6c gives a 3D perspective, showing a scaffold in a cuvette from two sides after printing and washing.

Microscopy and dimensional analyses revealed that the printed constructs systematically deviated from their digital counterparts, with average linear oversizing of approximately 13% for $7 \times 7 \times 3$ mm and 11% for $4 \times 4 \times 3$ mm scaffolds. This discrepancy may be attributed to light diffusion during the Xolography exposure process, and the threshold behavior of polymerization at microscale resolutions. Despite this, the printed scaffolds retained well-defined architectural features, including consistent strut connectivity and surface regularity, indicating high shape fidelity relative to the simplified models. In contrast, all osteoporotic-mimetic scaffold designs did not yield structurally stable printed parts. Their elevated porosity and reduced strut dimensions fell below the minimum threshold required for self-supporting structures.

3.6. CFD simulation results

CFD simulations were conducted under perfusion-like conditions representative of in vitro bioreactor environments (Fig. 7a). The WSS distribution on the scaffold surfaces was analysed, and scaffold permeability was also calculated.

WSS distributions highlighted the functional behavior of the scaffolds under simulated flow. Ranges known to elicit different effects on MSCs are shown in Fig. 7b. In healthy scaffold geometries, inlet velocities in the range of 0.15–0.25 mm/s produced surface WSS values within the osteogenic window (0.11–10 mPa), known to stimulate bone formation processes. These simulations yielded permeability values ranging from 3.54×10^{-8} to 19.0×10^{-8} m^2 across all scaffold configurations (Fig. 7c). Larger scaffolds consistently exhibit higher permeability compared to smaller ones, due to increased flow cross-sections and reduced hydraulic resistance. Within both healthy and osteoporotic design groups, permeability inversely correlated with the number of

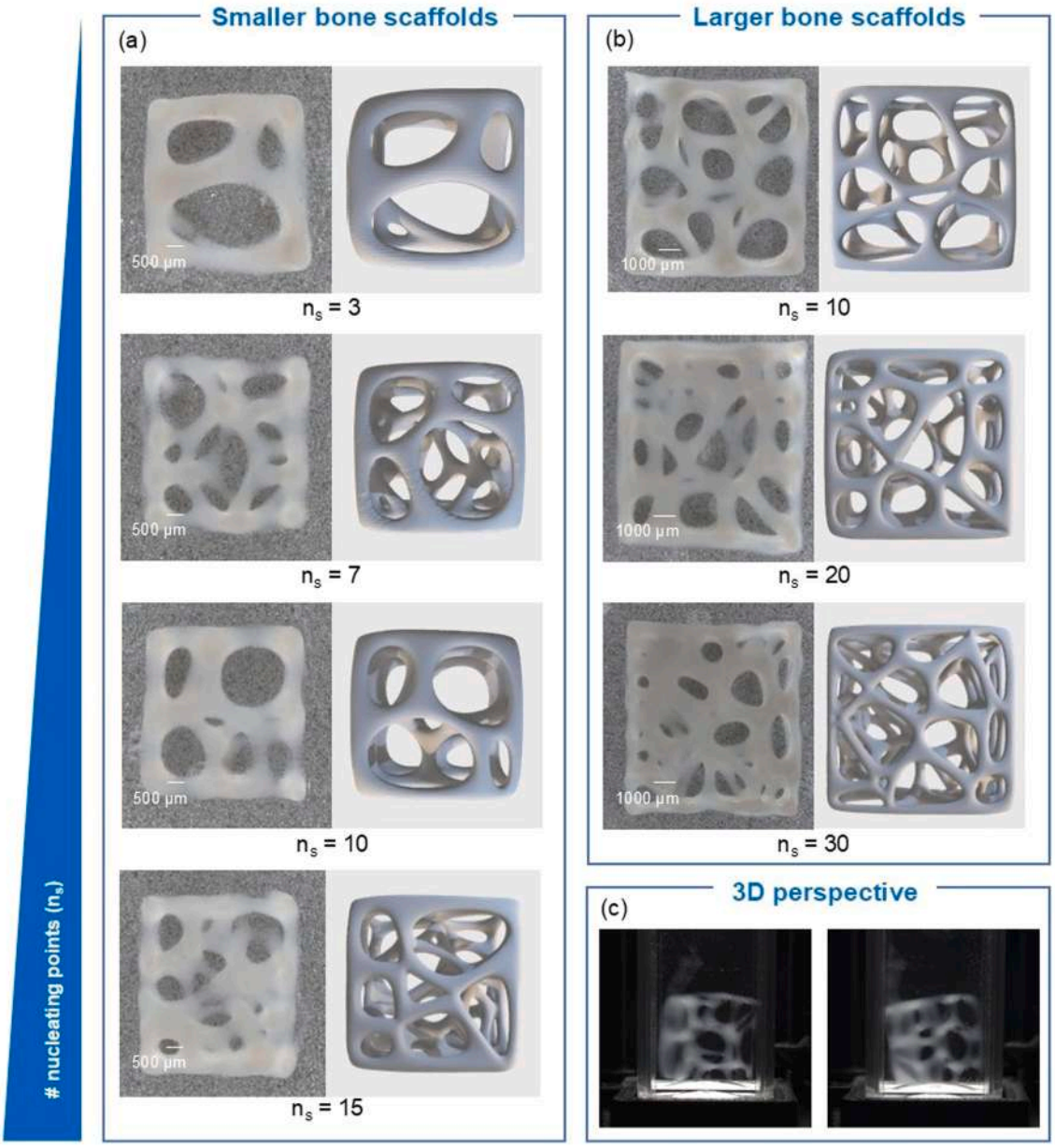

Fig. 6. Xolography printed scaffolds visualised with a digital microscope and their corresponding designs: (a) smaller size and (b) larger size. (c) Exemplary scaffold in a cuvette after printing and washing, showing the 3D structure from two sides.

nucleating points. Osteoporotic-mimetic scaffolds showed overall higher permeability than healthy counterparts. This observation was consistent with their greater porosity and thinner struts, which reduced resistance to interstitial flow.

WSS heatmaps (two representative samples per group are shown in Fig. 7d; the full dataset is available in Figs. S1–S2, Supporting Information) reveal spatial heterogeneity, with distinct regions experiencing WSS between 0.11–0.55 mPa, associated with osteogenic stimulation without mineralization, and regions exceeding 0.55 mPa, which are conducive to both osteogenesis and mineral deposition [20]. The percentage quantification of the surface area exposed to each WSS range for the different groups is reported in Fig. 7e. As the number of nucleating points increased, the proportion of scaffold surface area exposed to WSS values > 0.55 mPa also increased. Osteoporotic scaffolds subjected to identical flow rates exhibited lower overall WSS, with broader regions restricted to the 0.11–0.55 mPa range.

The CFD results obtained from the bone sub-volumes are also presented in Fig. 7d-e and Fig. S3 in Supporting Information, using the same layout as employed for the designed scaffold geometries. CFD simulations were performed on a subset of bone samples (4 healthy and 4 osteoporotic) whose BV/TV closely matched the mean BV/TV of the corresponding healthy-like and osteoporotic-like scaffolds. Among the 10 healthy and 10 osteoporotic bone samples available, these 4 healthy and 4 osteoporotic had BV/TV values sufficiently close to the scaffold BV/TV to allow a direct comparison of WSS while holding porosity constant. This matching criterion was adopted to isolate the influence of the density on WSS relative to the native bone architecture, minimizing confounding effects due to differences in BV/TV. In bone samples, similar trends were observed in WSS distribution patterns, particularly in the proportion of surface areas exposed to low (blue) and intermediate (green) WSS values. When comparing the bone samples with the smaller scaffolds, the percentages of surface area exposed to mineralization-enhancing showed no statistically significant differences were found between WSS in healthy scaffolds (75.21% $\pm$ 9.47%) and

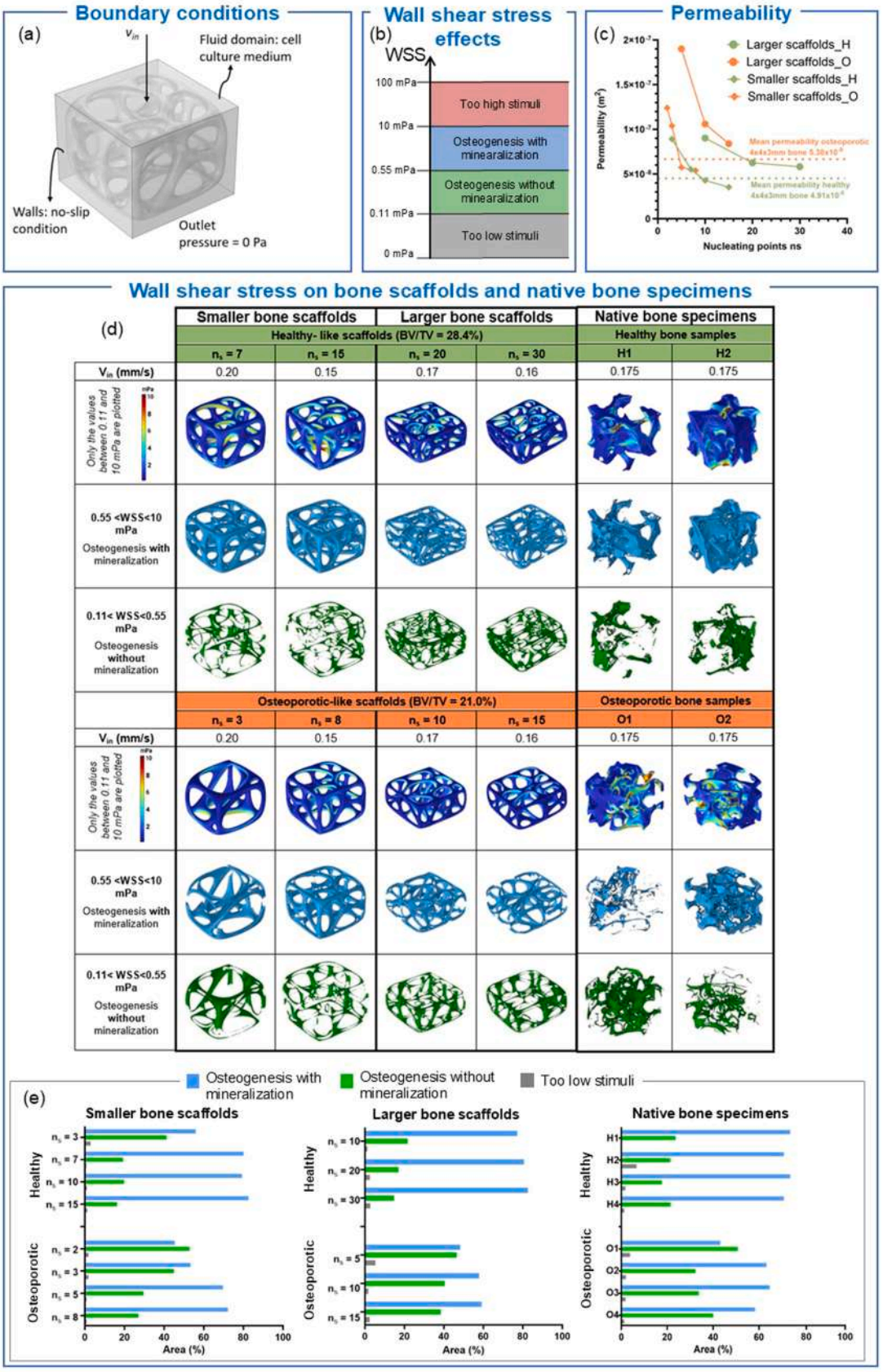

(caption on next page)

Fig. 7. Computational fluid dynamics (CFD) analysis on bone scaffolds and human bone specimens (a) CFD simulation domain and boundary conditions, modelling confined unidirectional perfusion through scaffold pores under bioreactor-like conditions. **(b)** Classification of wall shear stress (WSS) ranges based on osteogenic response of Mesenchymal Stem Cells: sub-threshold (non-stimulatory), osteoinductive without mineralization, and osteoinductive with enhanced mineralization. Adapted from Melke et al. [15] **(c)** Simulated permeability values as a function of geometrical complexity (nucleation points n_s), comparing scaffolds mimicking osteoporotic and healthy trabecular architectures across two scaffold sizes. **(d)** WSS distributions mapped onto scaffold surfaces and human bone specimen surfaces, highlighting areas subjected to osteogenesis-promoting WSS ranges: 0.11–1.5 mPa (green, without mineralization) and 1.5–10 mPa (blue, with enhanced mineralization). Two representative samples for each group are shown, the maps of all the samples are available in Fig. S1−2–3, Supplementary Information. **(e)** Quantitative analysis of surface area percentages exposed to different WSS ranges.

healthy bone (72.25% ± 1.38%) samples ($p = 0.343$) or between osteoporotic scaffolds (69.09% ± 20.23%) and osteoporotic bone (57.34% ± 8.54%) samples ($p = 0.686$). These results suggest that the scaffolds successfully replicated the native WSS environment. In addition, average permeability values for the native bone samples were included in Fig. 7c: $5.38 \times 10^{-8} \pm 0.31 \times 10^{-8}$ m^2 for osteoporotic bone and $4.91 \times 10^{-8} \pm 0.20 \times 10^{-8}$ m^2 for healthy bone. These values were comparable to those observed in the scaffold series, particularly in the designs with a higher number of nucleating points. Moreover, the scaffolds reproduced the increased permeability characteristic of the osteoporotic case, consistent with native bone.

4. Discussion

4.1. Effects of osteoporosis on trabecular architecture and the translation of morphometric parameters into scaffold design

Osteoporosis was found to induce a statistically significant reduction in BV/TV, concomitant enlargement of trabecular spacing, and an increase in anisotropy index. These findings are in line with compromised trabecular integrity and increased fracture susceptibility by enhanced osteoclastic resorption that is outpacing osteoblastic formation as reported elsewhere [9,70,71]. The elevated heterogeneity in trabecular spacing observed among osteoporotic specimens is likely based on inter-subject variability in disease progression and mechanical loading conditions. The observed increase in anisotropy is hypothesised to result from the preferential resorption of trabeculae oriented orthogonally to the dominant load directions [70,71]. Conversely, trabecular thickness and connectivity density metrics did not display statistically significant differences between healthy and osteoporotic groups. This observation could be mechanistically rationalised by competing microarchitectural phenomena: progressive trabecular fragmentation induced by bone loss tends to reduce connectivity density, whereas concurrent remodelling processes induce a morphological transition from plate-like to rod-like trabecular elements (also with central plate perforation), which could partially enhance connectivity [9,70,72,73]. It must be noted, however, that, although the cohort was restricted to elderly female donors to reduce confounding, the relatively small sample size and the single anatomical source limit the generalizability of these findings to male donors, younger populations and other skeletal sites. Previous morphometric studies on human trabecular bone using CT- or synchrotron-based imaging have reported comparable sample sizes, supporting the feasibility of our approach within its limitations [9,54,57].

Three geometrical parameters (bone volume fraction, trabecular spacing, and trabecular thickness) were chosen as constraints to guide the scaffold design workflow. These descriptors captured the essential geometric determinants of trabecular bone functionality by balancing structural integrity and permeability. The employed generative approach ensured flexibility and scalability, as it can be applied to regions of interest of arbitrary shape and size. Furthermore, simple modification of the morphometric inputs enables efficient generation of geometries spanning both healthy and osteoporotic architectural regimes [64,74].

The final scaffold designs were produced in two different dimensions with topological complexity regulated through Voronoi nucleation density. Higher nucleation densities yielded increasingly intricate architectures characterised by finer features and reduced pore dimensions. The scaffolds matched the BV/TV of healthy and osteoporotic trabecular bone, but exhibited increased strut thickness and spacing, which progressively approached native values in the more complex architectures. Control over the design variations allowed here to investigate the influence of scaffold size and complexity on fluid transport *in silico* and could be adjusted to ensure manufacturability by accounting for resolution limits of manufacturing processes for in vitro studies.

4.2. Bone scaffolds manufacturing: introduction and characterization of new Xolography-printed hydrogels

The choice of the employed hydrogels was guided by the combined requirements of Xolography processing, prior literature evidence and the targeted scaffold design. Previous studies have demonstrated that Xolography enables high-resolution fabrication with synthetic photopolymers [26], [27] whereas biocompatible hydrogel systems remain comparatively underdeveloped. Cytocompatibility has mainly been reported for GelMA-based and GelMA–PEGDA formulations [28,38,39] which, however, exhibited lower print resolution than synthetic counterparts. [28,38,39]. Low molecular weight (M_n = 575 or 700) PEGDA-based systems enable higher printing resolution and more stable processing conditions, making them better suited for fabricating complex geometries required for this study, although they lack intrinsic bioactive motifs [28,38]. Higher-molecular-weight PEGDA improves cytocompatibility but compromises print resolution or processability [28,38]. To address this trade off, the rationale was to retain low molecular weight PEGDA (M_n =700) and replace GelMA with PEGDMA, which provided methacrylate functional groups amenable to conjugation with bioactive motifs such as the RGD peptides, a strategy previously used to enhance cell adhesion by facilitating integrin engagement [66]. Similar PEGDA/PEGDMA combinations have demonstrated improved biological performance in other photopolymerization techniques [66], although their application in Xolography remained unexplored.

Printing conditions varied for each hydrogel composition: the 40% PEGDA formulation supported low energy input, while increasing PEGDMA content required higher energy doses to achieve complete polymerization. This behavior is likely linked to distinct crosslinking kinetics of acrylate and methacrylate groups and is in agreement with Stoecker et al. [28], who observed slower printing dynamics in GelMA/PEGDA blends compared to pure PEGDA systems. Higher PEGDMA content required higher energy input which was accompanied by over-polymerization during extended exposure, leading to diminished resolution and geometric fidelity.

The stiffness measured via compression tests was primarily governed by the PEGDA:PEGDMA ratio: the Young's modulus decreases with increasing PEGDMA content, a trend previously reported by Anindita et al. [66]. While variations in printing parameters (speed, intensity and energy dose) were necessary to accommodate the specific 'printing window' of each formulation, these parameters did not show a standalone monotonic correlation with the compressive elastic modulus, as it happens for other 3D printing techniques and materials [75]. An exception was noted for the 40% PEGDMA formulation: the higher stiffness observed can be attributed to the significantly higher energy dose and slower printing speed required to achieve stable polymerization. This increased exposure likely enhanced the crosslinking density,

overriding the softening effect associated with higher PEGDMA percentages.

The measured stiffness from microindentation was significantly lower than that obtained from compression tests, particularly in the 30% PEGDA–10% PEGDMA and 40% PEGDMA samples. This discrepancy reflects the inherent difference in probed volume and loading mode which is correspondingly influenced by surface features, microstructure, and local crosslink density [76,77]. Across all compositions, microindentation results exhibited minimal spatial variability, indicating uniform curing throughout the printed structures. Overall, stiffness values ranged from 201 to 678 kPa, significantly lower than that of native trabecular bone (1–10 GPa) [78,79], but within a suitable range for samples in in vitro testing [80–82]. What is more, all hydrogel formulations maintained structural integrity and dimensional stability over time, with a swelling ratio near unity over 21 days in aqueous condition. This stable swelling behavior reflected robust crosslinking and resistance to osmotic expansion, supporting their use in sustained culture environments without significant geometric distortion.

As expected, the non-functionalised 40% PEGDA hydrogel, lacking methacrylate sites, showed the lowest metabolic activity of the groups compared. In contrast, PEGDMA-containing formulations displayed increased cell metabolic activity with and without RGD conjugation, demonstrating the biofunctionality of the methacrylate groups. The RGD-functionalised formulations achieved higher metabolic activities with the highest activity for the 40% PEGDMA formulation (~65% relative to control), though its limited printability restricts its application in complex scaffold fabrication. Presence of cells was confirmed with brightfield imaging for functionalized prints with the lowest concentration of PEGDMA, nevertheless, more spatial information about cell attachment and cellular morphology on these hydrogels should be obtained with immunofluorescent confocal microscopy.

Scaffolds modelled according to healthy bone morphology were successfully printed using the selected formulation of 30% PEGDA–10% PEGDMA which demonstrated a balance between print fidelity, mechanical competence, and metabolic activity. However, osteoporotic scaffold designs, characterised by higher porosity and lower connectivity, consistently failed to print, likely due to insufficient volume fraction. Notably, the herein investigated structures exceed the geometrical fragility of previous studies that demonstrated defined printability of equivalent or similar material formulations [28,38,39]. These findings underscore the need for further optimization of both design parameters and material formulations to fabricate scaffolds that replicate the structural characteristics of pathological bone tissue. Potential strategies to improve the printability include the addition of TEMPO as a radical scavenger to shift the processing window or adjustments of the temperature and viscosity of the resin during printing to influence reaction kinetics.

4.3. Interstitial fluid flow in designed bone scaffolds

To study the effect of osteoporotic degeneration in architecture on fluid flow, the same inlet fluid velocity was applied to all samples. It was iteratively tuned in healthy scaffolds to yield WSS values within osteogenic (0.11–10 mPa) and mineralization-favourable (>0.55 mPa) ranges and then applied also to osteoporotic scaffolds. These optimised velocities, typically between 0.15 and 0.25 mm/s, fell within the operational capacity of standard perfusion systems (e.g., syringe and peristaltic pumps), ensuring translational feasibility. Simulations confirmed that healthy bone-mimetic scaffolds exposed to these velocities generated widespread regions of osteoinductive shear stress, with significant surface areas exceeding the threshold for mineralization. This spatial distribution of WSS is critical, as localised variations could influence the spatial organization of bone matrix deposition and tissue integration. In contrast, osteoporotic scaffolds subjected to the same inlet velocities exhibited significantly reduced WSS magnitudes across their surfaces. Although portions of these geometries still experienced osteogenic WSS, the overall intensity and extent of mineralization-promoting regions were diminished. This outcome reflected the characteristic increase in porosity and strut spacing associated with osteoporotic trabecular architecture, which facilitated higher flow-through (i.e., increased permeability) but attenuated shear stress transmission due to reduced surface confinement. CFD simulations on the native bone scans revealed a clear similarity in WSS spatial distributions between native bone and the corresponding scaffold designs. In particular, the relative proportions of scaffold or bone surface exposed to osteogenic and mineralizing WSS ranges followed consistent trends across the two domains. Furthermore, permeability values in bone specimens closely matched those of high-density scaffold variants. These findings suggested that the generative approach did not only replicate the morphology of bone tissue but also successfully captured its key fluid-dynamic behavior under perfusion.

Key trends emerging from the simulations include:

i. ***Increased geometric complexity*** correlated with reduced permeability but promoted higher WSS heterogeneity and elevated peak values, which may enhance spatial control over osteogenic differentiation;
ii. ***Reducing scaffold dimensions*** resulted in lower permeability without markedly altering WSS distribution;
iii. ***Comparative analysis of healthy and osteoporotic scaffolds***, across both scaffold designs and native bone sub-volumes, revealed that osteoporotic samples yielded higher permeability but lower surface WSS, leading to insufficient mechanical stimulus for robust mineralization. This parallel behavior confirmed that the scaffolds not only mimic bone structure, but also recapitulated condition-specific fluid dynamics and stimulus transmission. The lower WSS observed in osteoporotic conditions as a consequence of bone loss may initiate a vicious circle since reduced mechanical stimulation of osteoblasts leads to impaired bone matrix deposition.

4.4. Conclusions

This study advances understanding of how trabecular architecture governs interstitial fluid flow in physiological and pathological states, revealing that osteoporotic bone exhibits higher permeability and lower wall shear stress than healthy bone, thus altering mechanically relevant cues for bone cells. As proof-of-concept, it demonstrates that integrating generative scaffold design and CFD simulations successfully translates key structural and fluid-dynamic features of healthy and diseased bone into simplified geometries that preserve functionally meaningful cellular stimuli through shear stress. To take a step toward experimental application, healthy bone-inspired scaffolds were printed via Xolography using PEG-based hydrogels suitable for cell culture and in vitro use, though osteoporotic designs proved challenging, necessitating printability optimizations. The natural next step is to experimentally validate cell behavior under dynamic culture conditions, thereby assessing the impact of these mechanically derived cues on cellular response. In addition, expanding the number of bone samples in the morphometric analysis would provide a more comprehensive characterization of osteoporosis-related structural variability.

Declaration of Competing Interest

The authors declare that they have no known competing financial interests or personal relationships that could have appeared to influence the work reported in this paper.

Acknowledgements

The authors acknowledge that the presented work was realised using the infrastructure provided by the Euro-BioImaging initiative

https://www.eurobioimaging.eu/

L.M., L.M.V, F.B. and M.C. acknowledge the financial support from the European Union Horizon Europe research and innovation programme under the Marie Skłodowska-Curie (MSCA) grant agreement No 101120290 (GAP).

Appendix A. Supporting information

Supplementary data associated with this article can be found in the online version at doi:10.1016/j.apmt.2026.103394.

References

[1] G. Zhu, et al., Bone physiological microenvironment and healing mechanism: basis for future bone-tissue engineering scaffolds, Bioact. Mater. 6 (11) (Nov. 2021) 4110–4140, https://doi.org/10.1016/j.bioactmat.2021.03.043.
[2] I. Sallent, et al., The few who made it: commercially and clinically successful innovative bone grafts, Front. Bioeng. Biotechnol. 8 (Sep. 2020), https://doi.org/10.3389/fbioe.2020.00952.
[3] G. Li, L. Thabane, A. Papaioannou, G. Ioannidis, M.A.H. Levine, J.D. Adachi, An overview of osteoporosis and frailty in the elderly, BMC Musculoskelet. Disord. 18 (2017), https://doi.org/10.1186/s12891-017-1403-x.
[4] N. Harvey, E. Dennison, C. Cooper, Osteoporosis: impact on health and economics, Nat. Rev. Rheumatol. 6 (2) (Feb. 2010) 99–105, https://doi.org/10.1038/nrrheum.2009.260.
[5] International Osteoporosis Foundation, 'Osteoporosis - Epidemiology', IOF. Accessed: Oct. 16, 2024. [Online]. Available: https://www.osteoporosis.foundation/health-professionals/about-osteoporosis/epidemiology.
[6] P. Zioupos, H.O.K. Kirchner, H. Peterlik, Ageing bone fractures: the case of a ductile to brittle transition that shifts with age, Bone 131 (Feb. 2020) 115176, https://doi.org/10.1016/j.bone.2019.115176.
[7] J.A. Kanis, et al., SCOPE 2021: a new scorecard for osteoporosis in Europe, Arch. Osteoporos. (Jun. 2021), https://doi.org/10.1007/s11657-020-00871-9.
[8] E. Hernlund, et al., Osteoporosis in the European Union: medical management, epidemiology and economic burden, Arch. Osteoporos. 8 (1) (Oct. 2013) 136, https://doi.org/10.1007/s11657-013-0136-1.
[9] C. Bregoli, C.A. Biffi, A. Tuissi, F. Buccino, Effect of trabecular architectures on the mechanical response in osteoporotic and healthy human bone, Med. Biol. Eng. Comput. (Jun. 2024), https://doi.org/10.1007/s11517-024-03134-8.
[10] T. Tang, T. Casagrande, P. Mohammadpour, W. Landis, B. Lievers, K. Grandfield, Characterization of human trabecular bone across multiple length scales using a correlative approach combining X-ray tomography with LaserFIB and plasma FIB-SEM, Sci. Rep. 14 (1) (Sep. 2024) 21604, https://doi.org/10.1038/s41598-024-72739-8.
[11] F. Cosmi, N. Steimberg, G. Mazzoleni, A mesoscale study of the degradation of bone structural properties in modeled microgravity conditions, J. Mech. Behav. Biomed. Mater. 44 (Apr. 2015) 61–70, https://doi.org/10.1016/j.jmbbm.2015.01.002.
[12] C. Nguyen, et al., Novel magnetic resonance technique for characterizing mesoscale structure of trabecular bone, R. Soc. Open. Sci. 5 (8) (Aug. 2018) 180563, https://doi.org/10.1098/rsos.180563.
[13] F. Xie, et al., Microstructural properties of trabecular bone autografts: comparison of men and women with and without osteoporosis, Arch. Osteoporos. 13 (1) (Mar. 2018) 18, https://doi.org/10.1007/s11657-018-0422-z.
[14] A. Muñoz, A. De Paolis, L. Cardoso, A. Carriero, Osteocyte-lacuna shape and canaliculi architecture dictate fluid flow around osteocyte, and strain of cell and bone matrix: implications for cell mechanobiology and bone fragility, Bone 200 (Nov. 2025) 117613, https://doi.org/10.1016/j.bone.2025.117613.
[15] C. Price, X. Zhou, W. Li, L. Wang, Real-time measurement of solute transport within the lacunar-canalicular system of mechanically loaded bone: Direct evidence for load-induced fluid flow, J. Bone Miner. Res. 26 (2) (2011) 277–285, https://doi.org/10.1002/jbmr.211.
[16] A.F. van Tol, et al., The mechanoresponse of bone is closely related to the osteocyte lacunocanalicular network architecture, Proc. Natl. Acad. Sci. 117 (51) (Dec. 2020) 32251–32259, https://doi.org/10.1073/pnas.2011504117.
[17] T.A. Metzger, S.A. Schwaner, A.J. LaNeve, T.C. Kreipke, G.L. Niebur, Pressure and shear stress in trabecular bone marrow during whole bone loading, J. Biomech. 48 (12) (Sep. 2015) 3035–3043, https://doi.org/10.1016/j.jbiomech.2015.07.028.
[18] T. Adachi, Y. Kameo, M. Hojo, Trabecular bone remodelling simulation considering osteocytic response to fluid-induced shear stress, ' Philos. Trans. R. Soc. Math. Phys. Eng. Sci. 368 (1920) (Jun. 2010) 2669–2682, https://doi.org/10.1098/rsta.2010.0073.
[19] T. Li, et al., Fluid–solid coupling numerical simulation of trabecular bone under cyclic loading in different directions, J. Biomech. 109 (Jul. 2020) 109912, https://doi.org/10.1016/j.jbiomech.2020.109912.
[20] J. Melke, F. Zhao, B. Rietbergen, K. Ito, S. Hofmann, Localisation of mineralised tissue in a complex spinner flask environment correlates with predicted wall shear stress level localisation, Eur. Cell. Mater. 36 (Jul. 2018) 57–68, https://doi.org/10.22203/eCM.v036a05.
[21] R. Xue, S. Cartmell, A simple in vitro biomimetic perfusion system for mechanotransduction study, Sci. Technol. Adv. Mater. 21 (1) (Sep. 2020) 635–640, https://doi.org/10.1080/14686996.2020.1808432.
[22] Y. Sun, et al., Mechanical stimulation on mesenchymal stem cells and surrounding microenvironments in bone regeneration: regulations and applications, Front. Cell. Dev. Biol. 10 (Jan. 2022), https://doi.org/10.3389/fcell.2022.808303.
[23] A.B. Yeatts, J.P. Fisher, Bone tissue engineering bioreactors: dynamic culture and the influence of shear stress, Bone 48 (2) (Oct. 2011) 171–181, https://doi.org/10.1016/j.bone.2010.09.138.
[24] S. Zhao, Z. Chen, T. Li, Q. Sun, H. Leng, B. Huo, Numerical simulations of fluid flow in trabecular–lacunar cavities under cyclic loading, Comput. Biol. Med. 163 (Sep. 2023) 107144, https://doi.org/10.1016/j.compbiomed.2023.107144.
[25] S. O'Halloran, A. Pandit, A. Heise, A. Kellett, Two-photon polymerization: fundamentals, materials, and chemical modification strategies, Adv. Sci. 10 (7) (2023) 2204072, https://doi.org/10.1002/advs.202204072.
[26] M. Regehly, et al., Xolography for linear volumetric 3D printing, Nature 588 (7839) (Dec. 2020) 620–624, https://doi.org/10.1038/s41586-020-3029-7.
[27] L. Stüwe, et al., Continuous Volumetric 3D Printing: Xolography in Flow, Adv. Mater. 36 (4) (2024) 2306716, https://doi.org/10.1002/adma.202306716.
[28] L. Stoecker, et al., Xolography for Biomedical Applications: Dual-Color Light-Sheet Printing of Hydrogels With Local Control Over Shape and Stiffness, Adv. Mater. 37 (10) (2025) 2410292, https://doi.org/10.1002/adma.202410292.
[29] X. Guo, J. Li, Y. Wu, L. Xu, Recent advancements in hydrogels as novel tissue engineering scaffolds for dental pulp regeneration, Int. J. Biol. Macromol. 264 (Apr. 2024) 130708, https://doi.org/10.1016/j.ijbiomac.2024.130708.
[30] H. Yang, et al., Recent progress on functional hydrogels as biomaterial for biomedicine, ' Results Chem. 16 (Jul. 2025) 102464, https://doi.org/10.1016/j.rechem.2025.102464.
[31] W. Wang, T. Cai, C. Shao, Y. Xiao, Y. Xiang, Y. Jiang, MXene-Based Responsive Hydrogels and Applications in Wound Healing, ChemistrySelect 9 (32) (2024) e202402073, https://doi.org/10.1002/slct.202402073.
[32] K. Zöller, D. To, A. Bernkop-Schnürch, Biomedical applications of functional hydrogels: Innovative developments, relevant clinical trials and advanced products, Biomaterials 312 (Jan. 2025) 122718, https://doi.org/10.1016/j.biomaterials.2024.122718.
[33] Z. Xiang, et al., Gelatin/heparin coated bio-inspired polyurethane composite fibers to construct small-caliber artificial blood vessel grafts, Int. J. Biol. Macromol. 269 (Jun. 2024) 131849, https://doi.org/10.1016/j.ijbiomac.2024.131849.
[34] S. Cheng, et al., A motion-responsive injectable lubricative hydrogel for efficient Achilles tendon adhesion prevention, Mater. Today Bio 30 (Feb. 2025) 101458, https://doi.org/10.1016/j.mtbio.2025.101458.
[35] L. Guida, M. Cavallaro, M. Levi, Advancements in high-resolution 3D bioprinting: Exploring technological trends, bioinks and achieved resolutions, Bioprinting 44 (Dec. 2024) e00376, https://doi.org/10.1016/j.bprint.2024.e00376.
[36] M. Kazemi, S. Maralbashi, Advances in 3D bioprinting for medical application: opportunities and challenges, Biomed. Eng. OnLine 25 (1) (Dec. 2025) 11, https://doi.org/10.1186/s12938-025-01498-y.
[37] R. Liu, et al., Chondrocyte spheroid-laden microporous hydrogel-based 3D bioprinting for cartilage regeneration, Int. J. Bioprinting 0 (0) (Jul. 2023) 0161, https://doi.org/10.36922/ijb.0161.
[38] A. Wolfel, et al., Bioxolography Using Diphenyliodonium Chloride and N-Vinylpyrrolidone Enables Rapid High-Resolution Volumetric 3D Printing of Spatially Encoded Living Matter, Adv. Mater. 37 (37) (2025) 2501052, https://doi.org/10.1002/adma.202501052.
[39] E. Brauer *et al.*, 'Biocompatible Ink Optimization Enables Functional Volumetric Bioprinting With Xolography', *Adv. Mater.*, p. e12058, doi: 10.1002/adma.202512058.
[40] WHO, Assessment of fracture risk and its application to screening for Postmenopausal Osteoporosis, World Health Organization,, Geneva, 1994.
[41] A. Abrami, et al., Medical applications of synchrotron radiation at the SYRMEP beamline of ELETTRA, ' Nucl. Instrum. Methods Phys. Res. Sect. Accel. Spectrometers Detect. Assoc. Equip. 548 (1–2) (Apr. 2005) 221–227, https://doi.org/10.1016/j.nima.2005.03.093.
[42] 'SYRMEP beamline description', Elettra Sincrotrone Trieste. Accessed: Oct. 28, 2024. [Online]. Available: https://www.elettra.eu/lightsources/elettra/elettra-beamlines/syrmep/beamline-description.html.
[43] D. Paganin, S.C. Mayo, T.E. Gureyev, P.R. Miller, S.W. Wilkins, Simultaneous phase and amplitude extraction from a single defocused image of a homogeneous object, J. Microsc. 206 (1) (Apr. 2002) 33–40, https://doi.org/10.1046/j.1365-2818.2002.01010.x.
[44] F. Brun, et al., Enhanced and Flexible Software Tools for X-ray Computed Tomography at the Italian Synchrotron Radiation Facility Elettra, Fundam. Inform. (Oct. 2015) 233–243, https://doi.org/10.3233/FI-2015-1273.
[45] F. Buccino, et al., Assessing the intimate mechanobiological link between human bone micro-scale trabecular architecture and micro-damages, Eng. Fract. Mech. 270 (May 2022) 108582, https://doi.org/10.1016/j.engfracmech.2022.108582.
[46] L. Clementini, et al., Multifunctional in situ imaging of biological materials under load: A synchrotron-based platform for large-scale image-guided failure analysis, Mater. Des. 257 (Sep. 2025) 114408, https://doi.org/10.1016/j.matdes.2025.114408.
[47] P. Cignoni, M. Callieri, M. Corsini, M. Dellepiane, F. Ganovelli, G. Ranzuglia, MeshLab: an Open-Source Mesh Processing Tool, Eurographics Assoc,, 2008.
[48] R. Domander, A.A. Felder, M. Doube, BoneJ2 - refactoring established research software, Wellcome Open. Res. 6 (Apr. 2021) 37, https://doi.org/10.12688/wellcomeopenres.16619.2.
[49] T. Hildebrand, P. Rüegsegger, A new method for the model-independent assessment of thickness in three-dimensional images, J. Microsc. 185 (1) (1997) 67–75, https://doi.org/10.1046/j.1365-2818.1997.1340694.x.

[50] R. Dougherty, K.-H. Kunzelmann, Computing Local Thickness of 3D Structures with ImageJ, Microsc. Microanal. 13 (S02) (Aug. 2007), https://doi.org/10.1017/S1431927607074430.
[51] A. Odgaard, H.J.G. Gundersen, Quantification of connectivity in cancellous bone, with special emphasis on 3-D reconstructions, Bone 14 (2) (Mar. 1993) 173–182, https://doi.org/10.1016/8756-3282(93)90245-6.
[52] J. Toriwaki, T. Yonekura, Euler number and connectivity indexes of a three dimensional digital picture', Forma 17 (Jan. 2002) 183–209.
[53] T.P. Harrigan, R.W. Mann, Characterization of microstructural anisotropy in orthotropic materials using a second rank tensor, J. Mater. Sci. 19 (3) (Mar. 1984) 761–767, https://doi.org/10.1007/BF00540446.
[54] C. Chappard, et al., Subchondral bone micro-architectural alterations in osteoarthritis: a synchrotron micro-computed tomography study, Osteoarthr. Cartil. 14 (3) (Mar. 2006) 215–223, https://doi.org/10.1016/j.joca.2005.09.008.
[55] D. Ulrich, B. van Rietbergen, A. Laib, P. Ruegsegger, The ability of three-dimensional structural indices to reflect mechanical aspects of trabecular bone, Bone 25 (1) (Jul. 1999) 55–60, https://doi.org/10.1016/S8756-3282(99)00098-8.
[56] R. Rieger, J.C. Auregan, T. Hoc, Micro-finite-element method to assess elastic properties of trabecular bone at micro- and macroscopic level, Morphologie 102 (336) (Mar. 2018) 12–20, https://doi.org/10.1016/j.morpho.2017.07.175.
[57] S. Tassani, C. Öhman, M. Baleani, F. Baruffaldi, M. Viceconti, Anisotropy and inhomogeneity of the trabecular structure can describe the mechanical strength of osteoarthritic cancellous bone, J. Biomech. 43 (6) (Apr. 2010) 1160–1166, https://doi.org/10.1016/j.jbiomech.2009.11.034.
[58] Z. Xiong, et al., A New Microarchitecture-Based Parameter to Predict the Micromechanical Properties of Bone Allografts, Materials 16 (9) (Jan. 2023) 3349, https://doi.org/10.3390/ma16093349.
[59] M. Ding, A. Odgaard, C.C. Danielsen, I. Hvid, Mutual associations among microstructural, physical and mechanical properties of human cancellous bone, J. Bone Jt. Surg. Br. 84-B (6) (Aug. 2002) 900–907, https://doi.org/10.1302/0301-620X.84B6.0840900.
[60] A.S. El-Gizawy, X. Ma, F. Pfeiffer, J.D. Schiffbauer, T. Selly, Characterization of Microarchitectures, Stiffness and Strength of Human Trabecular Bone Using Micro-Computed Tomography (Micro-CT) Scans, BioMed 3 (1) (Mar. 2023) 89–100, https://doi.org/10.3390/biomed3010007.
[61] M. Senechal, A. Okabe, B. Boots, K. Sugihara, Spatial Tessellations: Concepts and Applications of Voronoi Diagrams, Coll. Math. J. 26 (1) (Jan. 1995) 79–81, https://doi.org/10.2307/2687299.
[62] Z. Zhao, J. Li, D. Yao, Y. Wei, Mechanical and permeability properties of porous scaffolds developed by a Voronoi tessellation for bone tissue engineering, J. Mater. Chem. B 10 (46) (Nov. 2022) 9699–9712, https://doi.org/10.1039/D2TB01478E.
[63] F.S. Bellelli, 'The fascinating world of Voronoi diagrams', F.S.Bellelli. Accessed: Nov. 03, 2024. [Online]. Available: https://fbellelli.com/posts/2021–07-08-the-fascinating-world-of-voronoi-diagrams/.
[64] M. Fantini, M. Curto, Interactive design and manufacturing of a Voronoi-based biomimetic bone scaffold for morphological characterization allowed reproducing the actual architecture of the trabecular bone and could be suitable for Bone Tissue Engineering, according to specific surgical requirements.', Int. J. Interact. Manuf. 12 (2018) 585–596, https://doi.org/10.1007/s12008-017-0416-x.
[65] S. Huth, S. Sindt, C. Selhuber-Unkel, Automated analysis of soft hydrogel microindentation: Impact of various indentation parameters on the measurement of Young's modulus, PLOS ONE 14 (8) (Aug. 2019), https://doi.org/10.1371/journal.pone.0220281.
[66] S.N. Anindita, et al., Tough PEG-only hydrogels with complex 3D structure enabled by digital light processing of "all-PEG" resins, Aggregate 4 (6) (2023) e368, https://doi.org/10.1002/agt2.368.
[67] S. Gómez, M.D. Vlad, J. López, E. Fernández, Design and properties of 3D scaffolds for bone tissue engineering, Acta Biomater. 42 (Sep. 2016) 341–350, https://doi.org/10.1016/j.actbio.2016.06.032.
[68] P. Azizi, C. Drobek, H. Seitz, Numerical study of the structural design influence on cartilage cell differentiation in mechanically stimulated hydrogel scaffolds using an FSI-based model, Biomech. Model. Mechanobiol. 24 (4) (2025) 1417–1433, https://doi.org/10.1007/s10237-025-01976-1.
[69] J. Grenier, B. David, C. Journé, I. Cicha, D. Letourneur, H. Duval, Perfusion of MC3T3E1 Preosteoblast Spheroids within Polysaccharide-Based Hydrogel Scaffolds: An Experimental and Numerical Study at the Bioreactor Scale, Bioengineering 10 (7) (Jul. 2023) 849, https://doi.org/10.3390/bioengineering10070849.
[70] G. Molino, et al., Osteoporosis-related variations of trabecular bone properties of proximal human humeral heads at different scale lengths, J. Mech. Behav. Biomed. Mater. 100 (Dec. 2019) 103373, https://doi.org/10.1016/j.jmbbm.2019.103373.
[71] C. Chappard, et al., Anisotropy changes in post-menopausal osteoporosis: characterization by a new index applied to trabecular bone radiographic images, Osteoporos. Int. 16 (10) (Oct. 2005) 1193–1202, https://doi.org/10.1007/s00198-004-1829-5.
[72] G. Osterhoff, E.F. Morgan, S.J. Shefelbine, L. Karim, L.M. McNamara, P. Augat, Bone mechanical properties and changes with osteoporosis, no. Suppl 2, Injury 47 (Jun. 2016) S11–S20, https://doi.org/10.1016/S0020-1383(16)47003-8.
[73] A.M. Parfitt, C.H. Mathews, A.R. Villanueva, M. Kleerekoper, B. Frame, D.S. Rao, Relationships between surface, volume, and thickness of iliac trabecular bone in aging and in osteoporosis. Implications for the microanatomic and cellular mechanisms of bone loss, J. Clin. Invest. 72 (4) (Oct. 1983) 1396–1409, https://doi.org/10.1172/JCI111096.
[74] K. Shea, R. Aish, M. Gourtovaia, Towards integrated performance-driven generative design tools, ' Autom. Constr. 14 (Mar. 2005) 553–560, https://doi.org/10.1016/j.autcon.2004.07.002.
[75] Y. Li, X. Han, Z. Ma, Research on the mechanical properties of PEEK material artificial bone implants fabricated by high-temperature air-assisted 3D printing, J. Mech. Behav. Biomed. Mater. 173 (Jan. 2026) 107207, https://doi.org/10.1016/j.jmbbm.2025.107207.
[76] M.H. Leite, F. Ferland, Determination of unconfined compressive strength and Young's modulus of porous materials by indentation tests, Eng. Geol. 59 (3) (Apr. 2001) 267–280, https://doi.org/10.1016/S0013-7952(00)00081-8.
[77] W. Cook, M. Hood, F. Tsai, Observations of crack growth in hard rock loaded by an indenter, ' Lnt J. Rock. Mech. Mm Sct Geomech. Abstr. 21 (2) (1984) 97–107.
[78] E.F. Morgan, G.U. Unnikrisnan, A.I. Hussein, Bone mechanical properties in healthy and diseased states, Annu. Rev. Biomed. Eng. 20 (Jun. 2018) 119–143, https://doi.org/10.1146/annurev-bioeng-062117-121139.
[79] M.M. Barak, Cortical and trabecular bone modeling and implications for bone functional adaptation in the mammalian tibia, Bioengineering 11 (5) (May 2024), https://doi.org/10.3390/bioengineering11050514.
[80] W.-T. Hsieh, Y.-S. Liu, Y. Lee, M.G. Rimando, K. Lin, O.K. Lee, Matrix dimensionality and stiffness cooperatively regulate osteogenesis of mesenchymal stromal cells, Acta Biomater. 32 (Mar. 2016) 210–222, https://doi.org/10.1016/j.actbio.2016.01.010.
[81] J. Lee, A.A. Abdeen, T.H. Huang, K.A. Kilian, Controlling cell geometry on substrates of variable stiffness can tune the degree of osteogenesis in human mesenchymal stem cells, J. Mech. Behav. Biomed. Mater. 38 (Oct. 2014) 209–218, https://doi.org/10.1016/j.jmbbm.2014.01.009.
[82] T. Zhang, et al., Regulating osteogenesis and adipogenesis in adipose-derived stem cells by controlling underlying substrate stiffness, J. Cell. Physiol. 233 (4) (2018) 3418–3428, https://doi.org/10.1002/jcp.26193.